

Uncertainty-Aware Validation Benchmarks for Coupling Free Flow and Porous-Medium Flow

Farid Mohammadi¹, Elissa Eggenweiler², Bernd Flemisch¹, Sergey Oladyshkin¹, Iryna Rybak², Martin Schneider¹, Kilian Weishaupt¹

¹University of Stuttgart, Institute for Modelling Hydraulic and Environmental Systems
Pfaffenwaldring 61, 70569 Stuttgart, Germany

²University of Stuttgart, Institute of Applied Analysis and Numerical Simulation
Pfaffenwaldring 57, 70569 Stuttgart, Germany

Key Points:

- An uncertainty-aware validation of three models coupling free flow and porous-medium flow is performed.
- A Bayesian framework is introduced and employed to validate and compare the performance of models against a pore-scale reference solution.
- We found that the Stokes–Darcy model with generalized interface conditions is the most accurate REV-scale model considered in this work.

Abstract

The correct choice of interface conditions and proper model parameters for coupled free-flow and porous-medium systems is vital for physically consistent modeling and accurate numerical simulations of applications. We apply the Stokes equations to describe the free flow and consider different models for both the porous-medium compartment and the coupling at the fluid–porous interface. These models are the REV-scale porous-medium model in the form of Darcy’s law with classical or generalized interface conditions and the pore-network model with its related coupling approach. We study the coupled flow problems’ behaviors considering a benchmark case, where a pore-scale resolved model provides the reference solution, and quantify the uncertainties in the models’ parameters and the reference data. For this purpose, we apply a statistical framework that incorporates a probabilistic modeling technique using a fully Bayesian approach. A Bayesian perspective on a validation task yields an optimal bias-variance trade-off against the reference data. It provides an integrative metric for model validation that incorporates parameter and conceptual uncertainty. Additionally, a model reduction technique, namely Bayesian Sparse Polynomial Chaos Expansion, is employed to accelerate the calibration and validation processes for the computationally demanding free-flow and porous-medium models using different coupling strategies. We perform uncertainty-aware validation, demonstrate each model’s predictive capabilities, and make a probabilistic model comparison using a Bayesian validation metric.

1 Introduction

Coupled free-flow and porous-medium systems play a significant role in many industrial, environmental, and biological settings, e.g., fuel cells, water flows in karst aquifers, blood flows in vessels and living tissues. Flow interaction between the free-flow region and the porous-medium domain is extremely involved and strongly

Corresponding author: Farid Mohammadi, farid.mohammadi@iws.uni-stuttgart.de

interface-driven. Therefore, a physically consistent description of flow processes in the whole coupled system and especially near the interface is crucial for accurate numerical simulations of applications. A lot of effort has been made during the last decades in mathematical modeling and analysis of such coupled flow systems, and several coupling strategies have been proposed (e.g., Angot et al., 2017; Discacciati & Quarteroni, 2009; Goyeau et al., 2003; Jäger & Mikelić, 2009; Lācis & Bagheri, 2017; Ochoa-Tapia & Whitaker, 1995; Eggenweiler & Rybak, 2021). The most widely studied coupled flow problem in the literature is the Stokes–Darcy problem. In this case, the Stokes equations describe the flow in the free-flow domain, Darcy’s law is used to model the fluid flow through the porous medium, and a set of coupling conditions is imposed on the fluid–porous interface.

The classical set of interface conditions (ICs), most often applied for the Stokes–Darcy coupling, contains a version of the Beavers–Joseph condition which was postulated for parallel flows to the porous layer (Beavers & Joseph, 1967). Later, Saffman (Saffman, 1971) simplified this condition and the Beavers–Joseph–Saffman condition was confirmed by its rigorous derivation using the theory of homogenisation and boundary layers (Jäger & Mikelić, 2009; Saffman, 1971). Both the Beavers–Joseph condition and its modification by Saffman are not suitable for arbitrary flow directions (Eggenweiler & Rybak, 2020), however, they are routinely applied in the literature to multidimensional flows (Discacciati & Gerardo-Giorda, 2018; Hanspal et al., 2009). Coupled Stokes–Darcy models contain several unknown effective parameters that need to be determined before using the models for numerical simulations of applications. In this paper, we focus on four uncertain parameters in the classical coupled Stokes–Darcy model: the exact interface position, the Beavers–Joseph coefficient, the permeability tensor and the maximum boundary velocity at the inflow boundary. The exact location of the fluid–porous interface for REV-scale models is not known a priori. In the literature, there are several recommendations to impose the sharp fluid–porous interface directly on the top of solid inclusions in case of circular grains (Lācis et al., 2020; Rybak et al., 2021; Beavers & Joseph, 1967). For other pore geometries, especially in the case of anisotropic media, the problem of optimal interface location is still open. However, the exact interface location is very important, especially for microfluidic models (Terzis et al., 2019) which are routinely used in experiments. Another uncertain parameter is the Beavers–Joseph coefficient α_{BJ} , which is supposed to contain the information on the surface roughness (Beavers & Joseph, 1967; Le Bars & Worster, 2006). An investigation to calibrate this parameter was recently carried out in (Rybak et al., 2021), however, only for isotropic media. There was also an attempt to determine the Beavers–Joseph coefficient experimentally for flows parallel to the fluid–porous interface, isotropic and orthotropic porous media (Mierzwiczak et al., 2019), where the Beavers–Joseph parameter was found to be $\alpha_{BJ} < 1$ and dependent on the intrinsic permeability. Yang et al. (2019) demonstrate that α_{BJ} should not be constant but vary along the interface depending on the flow direction near the porous bed. Finally, the permeability tensor appearing in the Beavers–Joseph condition is not necessarily the permeability of the porous bulk, as in the standard models (Discacciati et al., 2002; Discacciati & Quarteroni, 2009), but could also be permeability of the near-interfacial region (Lācis & Bagheri, 2017; Zampogna & Bottaro, 2016). We study the three discussed uncertain parameters in this manuscript for a specific geometrical configuration. Moreover, we compare the classical REV-scale model against two other coupled flow models: the Stokes–Darcy model with generalized interface conditions and the Stokes/pore-network model with its corresponding coupling approach.

For the generalized coupling conditions derived rigorously in (Eggenweiler & Rybak, 2021), the interface can be located at the distance $\mathcal{O}(\ell)$ from the top of the first row of solid inclusions, where ℓ denotes the characteristic pore size. Based on the chosen interface position and the pore geometry, the effective coefficients appearing in the new conditions are computed numerically using the theory of homogenization

and boundary layers (Carraro et al., 2015; Hornung, 1997; Jäger & Mikelić, 2000, 2009). This is the main advantage of the generalized interface conditions, besides their suitability for arbitrary flows in coupled Stokes–Darcy systems. These recently derived conditions are used for the comparison with the classical interface conditions and the pore-network model. There are other alternative coupling concepts in the literature for Stokes–Darcy problems (e.g., Angot et al., 2017, 2021; Lācis et al., 2020; Ochoa-Tapia & Whitaker, 1995), which are beyond the scope of this study. Pore-network models (Blunt, 2017) consider a simplified yet equivalent representation of the porous geometry by separating the void space into larger pore bodies connected by narrow pore throats. Despite their low computational demand, a rather high degree of pore-scale accuracy can be achieved (Oostrom et al., 2016). Pore-network models can also be combined with modeling approaches on different scales (Scheibe et al., 2015), such as Darcy-type continuum models (Balhoff, Thompson, & Hjortsø, 2007; Balhoff, Thomas, & Wheeler, 2007; Mehmani & Balhoff, 2014) or free-flow models (Beyhaghi et al., 2016). Weishaupt et al. (2019) developed a fully implicit, monolithic approach to couple a pore-network model with a (Navier–)Stokes model, which was later improved by considering pore-scale slip (Weishaupt et al., 2020).

According to the discussion above, there are various possibilities to conceptualize the coupling of free flow and porous-medium flow that could be seen as conceptual uncertainty. This conceptual uncertainty is mainly related to the description of processes in the porous medium and near the interface, for which, different mathematical models and coupling strategies are considered. The free-flow conceptualization is based on the Stokes equations for all discussed models. However, the way these models simulate the fluid flow in the porous medium and in the neighborhood of the interface varies. Apart from the conceptual uncertainty, each computational model contains parametric uncertainty, such as material parameters, or interface location that should also be rigorously addressed. Therefore, a significant research challenge is to accurately assess competing modeling concepts and validate the corresponding computational models against an experiment or a reference solution. Following the guidelines for validation benchmarks in (Oberkampf & Roy, 2010; Oberkampf & Trucano, 2008), the most important scientific question to be addressed here is how to compare quantitatively the computational models. Each validation benchmark must declare one or more methods that should be employed for quantitative comparison. The development of such validation metrics is an active field of research. While being potentially applicable to many research areas, rigorously developed validation metrics have been applied to some of them only, such as computational fluid dynamics (Oberkampf & Barone, 2006), computational solid mechanics (Mahadevan & Rebba, 2005) or heat transfer (Hills, 2006). To the best of our knowledge, no rigorous development and application of uncertainty-aware validation has been performed for the coupling of free flow and porous-medium flow. To fill this gap, we employ an uncertainty-aware validation metric that relies on the Bayesian analysis of the competing models.

A Bayesian perspective on a validation task yields an optimal bias-variance trade-off against the experimental data or reference solution. It provides an integrative metric for model validation that incorporates parameter and conceptual uncertainty (Geman et al., 1992; Schöniger et al., 2014, 2015). Following the Bayesian model selection pathway, we employ the Bayesian model evidence (BME) as a validation score, indicating the quality of the analyzed physical models against the available experimental data or finely resolved reference solution. The probabilistic nature of the Bayesian technique requires propagating the parametric uncertainty through all competing models – i.e., a significant number of model evaluations – to reach statistical convergence. In practice, however, the computational complexity of the underlying computational model and the total available computational budget severely restrict the number of evaluations that one can perform. This challenge renders the brute-force computation of the BME value, required for the Bayesian validation framework

(BVF), infeasible. We replace each original computational model with its easy-to-evaluate surrogate in the Bayesian analysis. A surrogate assisted Bayesian analysis has been applied to many applications, including hydrology e.g., Yoon et al. (2022), sediment transport e.g., Mohammadi et al. (2018); Beckers et al. (2020), processes in subsurface reservoirs e.g., Bazargan et al. (2015); Bazargan and Christie (2017); Scheurer et al. (2021), subsurface flow models e.g., Elsheikh et al. (2014). A surrogate model's main goal is to replicate the behavior of the underlying physical models from a limited set of runs without sacrificing the accuracy.

For constructing a surrogate, a computational model should be evaluated using those sets of modeling parameters, out of various possibilities, that cover the parametric space as well as possible. The polynomial chaos expansion (PCE) (Wiener, 1938) or its extension toward arbitrary polynomial chaos expansion (aPCE) (Oladyshkin & Nowak, 2012) is a well-known and rigorous approach providing functional representations of stochastic quantities. However, not all expansion terms are relevant for the representation of the underlying physical processes, and employing the concept of sparsity can lead to zero values for many coefficients in the expansion (Tipping, 2001). There are many mathematical approaches when dealing with a regression problem, such as PCE representation, that lead to a sparse solution. These approaches have led to the emergence of numerous sparse solvers in the compressed sensing (Arjouni et al., 2017), as well as in the sparse PCE. Lüthen et al. (2021) provide a comprehensive survey of the proposed solvers in the context of PCE. Here, we employ Bayesian sparse aPCE denoted as BsaPCE, which is an extension of aPCE within a Bayesian framework by means of a Bayesian sparse learning method (Tipping & Faul, 2003). BsaPCE not only identifies the expansion terms, which capture the relevant features of the physical model, but it is also able to provide a probabilistic prediction, i.e., a prediction with the associated uncertainty. This prediction uncertainty can be used as the expected error occurring when replacing the original computational model by a possibly less accurate surrogate.

The rest of this paper is organized as follows. In Section 2, the mathematical and computational models are presented that are going to be evaluated by means of the proposed benchmark scenario. The Bayesian validation framework is introduced in Section 3. The benchmark scenario is described in Section 4, while Section 5 is devoted to a discussion of the application of the Bayesian model selection. We conclude the paper with a summary and conclusions in Section 6.

2 Mathematical and Computational Models

From a pore-scale perspective, we consider a two-dimensional flow domain Ω_{flow} consisting of a free-flow domain Ω_{ff} and the pore space Ω_{pore} of the porous medium. The porous-medium domain Ω_{pm} has a periodic structure composed by the repetition of the REV (scaled unit cell) $Y^\ell = (0, \ell) \times (0, \ell)$, where ℓ is the microscopic length scale (Figure 1, left). From a macroscopic point of view, the coupled domain $\Omega = \Omega_{\text{ff}} \cup \Omega_{\text{pm}}$ comprises the free-flow region Ω_{ff} and the porous-medium domain Ω_{pm} , separated by a sharp fluid-porous interface Γ (Figure 1, right).

We consider isothermal single-phase flow at low Reynolds numbers. The same fluid occupies the free-flow domain and fully saturates the porous medium. This fluid is supposed to be incompressible and to have constant viscosity. We consider a non-deformable porous medium leading to constant porosity.

2.1 Pore-scale Resolved Model

At the pore scale, fluid flow in the whole flow domain Ω_{flow} is governed by the Stokes equations,

$$\nabla \cdot \mathbf{v} = 0, \quad -\nabla \cdot \mathbf{T}(\mathbf{v}, p) = \mathbf{0} \quad \text{in } \Omega_{\text{flow}}, \quad (1)$$

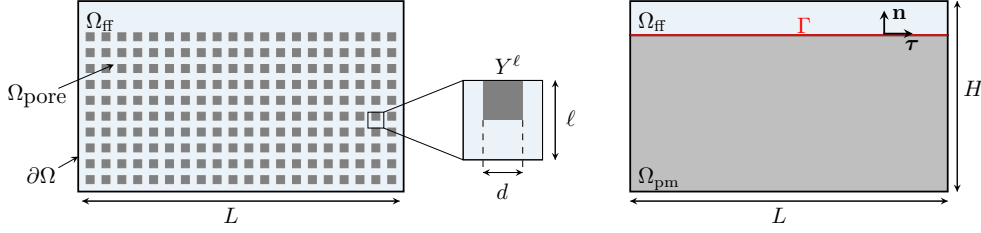


Figure 1. Geometrical setting at the pore scale (left) and REV scale (right).

completed with the no-slip condition on the boundary of solid inclusions

$$\mathbf{v} = \mathbf{0} \quad \text{on } \partial\Omega_{\text{flow}} \setminus \partial\Omega, \quad (2)$$

and appropriate conditions on the external boundary $\partial\Omega$. Here, \mathbf{v} and p denote the fluid velocity and pressure, $\mathbf{T}(\mathbf{v}, p) = \mu \nabla \mathbf{v} - p \mathbf{I}$ the stress tensor, \mathbf{I} the identity tensor and μ the dynamic viscosity.

Resolving pore-scale information is computationally expensive for practical applications. Therefore, REV-scale model formulations, which accurately reflect the pore-scale flow processes, are often preferred and are studied in this manuscript. The pore-scale resolved model (1)–(2) is used only for the model validation purposes in Section 4. A finite-volume scheme on staggered grids, also known as MAC scheme (Harlow & Welch, 1965), is used to discretize the pore-scale model (1)–(2).

2.2 Subdomain Models

In this study, we consider two different types of coupled models, for which the Stokes equations are used in the free-flow region Ω_{ff} but the porous domain Ω_{pm} is treated by different modeling concepts. The first type of model relies on the REV-scale description of the porous-medium domain using Darcy’s law, whereas the second type of model follows a hybrid-dimensional approach, where a lower-dimensional pore-network model is used to describe the fluid flow in the porous domain (Weishaupt et al., 2019, 2020).

Free flow. As a common feature, both coupled models (REV-scale model, pore-network model) contain the incompressible, stationary Stokes equations for the description of fluid flow in the free-flow domain

$$\nabla \cdot \mathbf{v}_{ff} = 0, \quad -\nabla \cdot \mathbf{T}(\mathbf{v}_{ff}, p_{ff}) = \mathbf{0} \quad \text{in } \Omega_{ff}, \quad (3)$$

where \mathbf{v}_{ff} is the fluid velocity and p_{ff} is the fluid pressure. For discretization of the Stokes system (3), the same MAC scheme as for model (1)–(2) is employed.

REV-scale porous-medium model. At the REV-scale, fluid flow through the porous medium is described by the Darcy flow equations

$$\nabla \cdot \mathbf{v}_{pm} = 0, \quad \mathbf{v}_{pm} = -\frac{\mathbf{K}}{\mu} \nabla p_{pm} \quad \text{in } \Omega_{pm}, \quad (4)$$

where \mathbf{v}_{pm} is the Darcy fluid velocity, p_{pm} is the fluid pressure and \mathbf{K} is the intrinsic permeability tensor, which is symmetric, positive definite, and bounded. Equations (4) are discretized with a vertex-centered finite-volume scheme, also known as box method (Hackbusch, 1989). This scheme has the advantage that degrees of freedom are naturally located at the interface and therefore directly allow the calculation of interfacial quantities (see Schneider et al. (2021) for more details) appearing in the coupling conditions (10)–(12) below.

Pore-network porous-medium model. For the pore-network model (PNM), we require the conservation of mass for each pore body i (the intersection of two or more pore throats):

$$\sum_j Q_{ij} = 0, \quad Q_{ij} = g_{ij}(p_i - p_j). \quad (5)$$

Here, Q_{ij} is the discrete volume flow rate in a throat connecting the pore bodies i and j , and the pressures defined at the centers of the pore bodies i and j are given by p_i and p_j (Figure 2). Equation (5) represents a finite-volume discretization scheme with a two-point flux approximation, see Weishaupt et al. (2020); Koch, Weishaupt, et al. (2021) for further details. The total conductance g_{ij} is determined by the pore throat geometry and the fluid properties. Considering the pressure losses both within the pore bodies and throats, we use

$$g_{ij} = (g_{t,ij}^{-1} + g_{p,i}^{-1} + g_{p,j}^{-1})^{-1}, \quad (6)$$

where $g_{t,ij}$ is the conductance of a throat ij while $g_{p,i}$ and $g_{p,j}$ are the conductances of the adjacent pore-body halves (Figure 2). Simple analytical expressions for g_{ij} are available in the literature (Patzek & Silin, 2001) for certain geometries. Usually, we determine g_{ij} via numerical upscaling (Mehmani & Tchelepi, 2017), whereas for this study, we consider it to be an additional uncertain parameter. In the following, we only refer to $g_{p,i}$, as for the given geometry $g_{p,i} = g_{p,j}$ for interior throats. At interface throats, one of the half-pore-body conductance is zero.

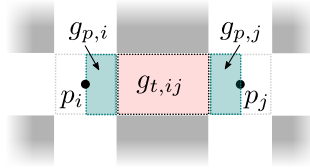


Figure 2. Schematic contribution to total conduction for the PNM. Throat ij connects the pore bodies i and j at the centers of which the pressures p_i and p_j are defined. $g_{t,ij}$ is the throat conductance valid for the region marked in light red. $g_{p,i}$ and $g_{p,j}$ are the conductances defined for the pore body halves marked in teal.

2.3 Coupling Concepts

A variety of REV-scale coupling concepts for the Stokes–Darcy system (3)–(4) is available in the literature. In this paper, we consider the most widely used set of interface conditions based on the Beavers–Joseph condition and recently developed generalized conditions (Eggenweiler & Rybak, 2021). If the pore-network model (5) is used in the porous medium, separate coupling conditions, suitable for the pore-scale description of interface exchange processes, must be considered.

Classical coupling conditions (REV-scale model). The most commonly used interface conditions are the *conservation of mass*

$$\mathbf{v}_{\text{ff}} \cdot \mathbf{n} = \mathbf{v}_{\text{pm}} \cdot \mathbf{n} \quad \text{on } \Gamma, \quad (7)$$

the *balance of normal forces*

$$-\mathbf{n} \cdot \mathbf{T}(\mathbf{v}_{\text{ff}}, p_{\text{ff}}) \mathbf{n} = p_{\text{pm}} \quad \text{on } \Gamma, \quad (8)$$

and the *Beavers–Joseph condition* (Beavers & Joseph, 1967) for the tangential component of velocity

$$(\mathbf{v}_{\text{ff}} - \mathbf{v}_{\text{pm}}) \cdot \boldsymbol{\tau} - \frac{\sqrt{\mathbf{K}}}{\alpha_{\text{BJ}}} \boldsymbol{\tau} \cdot \nabla \mathbf{v}_{\text{ff}} \mathbf{n} = 0 \quad \text{on } \Gamma. \quad (9)$$

Here, $\alpha_{BJ} > 0$ is the Beavers–Joseph parameter, \mathbf{n} is the normal unit vector on Γ pointing outward from the porous medium, $\boldsymbol{\tau}$ is a tangential unit vector on Γ and $\sqrt{\mathbf{K}} = \sqrt{\boldsymbol{\tau} \cdot \mathbf{K} \boldsymbol{\tau}}$ (Figure 1).

Although the classical coupling conditions (7)–(9) are unsuitable for arbitrary flows to the porous bed (Eggenweiler & Rybak, 2020), they are widely used in the literature for different flow scenarios.

Generalized coupling conditions for arbitrary flows (REV-scale model). Generalized interface conditions valid for arbitrary flow directions to the fluid–porous interface are rigorously derived in (Eggenweiler & Rybak, 2021) using the theory of homogenization and boundary layers. These conditions read

$$\mathbf{v}_{ff} \cdot \mathbf{n} = \mathbf{v}_{pm} \cdot \mathbf{n} \quad \text{on } \Gamma, \quad (10)$$

$$p_{pm} = -\mathbf{n} \cdot \mathbf{T}(\mathbf{v}_{ff}, p_{ff}) \mathbf{n} + \mu N_s^{bl} \boldsymbol{\tau} \cdot \nabla \mathbf{v}_{ff} \mathbf{n} \quad \text{on } \Gamma, \quad (11)$$

$$\mathbf{v}_{ff} \cdot \boldsymbol{\tau} = -\ell N_1^{bl} \boldsymbol{\tau} \cdot \nabla \mathbf{v}_{ff} \mathbf{n} + \mu^{-1} \ell^2 \sum_{j=1}^2 \frac{\partial p_{pm}}{\partial x_j} \mathbf{M}^{j,bl} \cdot \boldsymbol{\tau} \quad \text{on } \Gamma. \quad (12)$$

Here, $\mathbf{M}^{j,bl}$, N_1^{bl} and N_s^{bl} are boundary layer constants introduced in (Eggenweiler & Rybak, 2021), which are computed numerically based on the pore geometry.

Coupling conditions for the pore-network model. Each intersection of a pore body i with the free-flow domain boundary yields a pore-local discrete interface Γ_i on which we formulate coupling conditions (Figure 3). We assume no-flow/no-slip condition for the free flow at the location of solid grains (no intersecting pore throat). This results in the following coupling conditions for the free-flow/pore-network model

$$\mathbf{v}_{ff} \cdot \mathbf{n} = \mathbf{v}_{pm} \cdot \mathbf{n} \quad \text{on } \Gamma_i, \quad (13)$$

$$p_{pm} = p_{ff} \quad \text{on } \Gamma_i, \quad (14)$$

$$\mathbf{v}_{ff} \cdot \boldsymbol{\tau} = \begin{cases} v_{slip} & \text{on } \Gamma_i, \\ 0 & \text{else,} \end{cases} \quad (15)$$

with

$$v_{slip} = \frac{1}{\beta_{pore}} [(-(\nabla \mathbf{v} + \nabla \mathbf{v}^T) \mathbf{n}) \cdot \boldsymbol{\tau}]_{ff} + [\mathbf{v} \cdot \boldsymbol{\tau}]_{pm}. \quad (16)$$

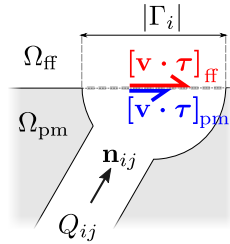


Figure 3. Schematic representation of local interface for the free-flow/pore-network model.

We approximate the tangential component of the pore-body interface velocity as

$$[\mathbf{v} \cdot \boldsymbol{\tau}]_{pm} = \frac{Q_{ij}}{|\Gamma_i|} [\mathbf{n}_{ij} \cdot \boldsymbol{\tau}]_{pm}, \quad (17)$$

where \mathbf{n}_{ij} is a unit normal vector parallel to the throat’s central axis and pointing towards the interface Γ_i . The volume flow through the pore throat ij is given by Q_{ij} and $|\Gamma_i|$ is the area of the discrete coupling interface.

Equations (15) and (16) can be seen as the pore-scale analog to Equation (9) with a pore-local slip coefficient β_{pore} , which is determined numerically in a preprocessing step. We refer to (Weishaupt et al., 2020) for more details. The three sets of coupling conditions (7)–(9), (10)–(12) and (13)–(15) listed above are discretized corresponding to the adjacent subdomain models’ discretizations, and the resulting coupled discrete models are treated by a monolithic strategy, assembling all contributions in a single system of equations for each model.

3 Bayesian Validation Framework

Several conceptual representations for the coupling of free flow and porous-medium flow have been presented in Section 2. In the current section, we offer a BVF to compare the models and validate related computational models, comparing their performance with respect to the best agreement to the pore-scale reference model. The benefits of this comparison are twofold. First, this evaluates the strengths and weaknesses of competing modeling concepts. Second, the predictive ability of each computational model is assessed. In terms of validation, we can define a hypothesis as to whether the models introduced in Sections 2.2 and 2.3 can, on the respective scale, satisfactorily represent the system of interest, provided by the pore-scale resolved model described in Section 2.1. Furthermore, we update the prior belief in the predictive capability of the models based on Bayesian notions. The resulting so-called posterior belief is expressed in terms of probabilities. The Bayesian approach in the task of validation allows us to include possible sources of errors that can lead to inevitable uncertainties. The BVF requires propagation of the parametric uncertainty through the given computationally demanding models. This propagation renders the analysis intractable, as it demands many model evaluations. To circumvent this problem, we employ a surrogate modeling technique to offset BVF’s computational time.

3.1 Bayesian Model Comparison

The topic of quantitative model comparison has received and continues to receive considerable attention in the field of statistics. There exist several multimodel comparison frameworks related to these model rating methods that allow for statistical model selection and averaging, e.g., (Gelman et al., 2013). The most common approach is Bayesian model selection (BMS) (Draper, 1995; Hoeting et al., 1999). BMS is grounded on Bayes’ theorem, which combines a prior belief about the efficiency of each model with its performance in replicating a common observation data set. Its procedure for model comparison entails principled and general solutions to the trade-off between parsimony and goodness-of-fit. Moreover, BMS is a formal statistical approach that allows comparing alternative conceptual models, testing their adequacy, combining their predictions into a more robust output estimate, and quantifying conceptual uncertainty’s contribution to the overall prediction uncertainty. BMS can be regarded as a Bayesian hypothesis testing framework, combining the idea of classical hypothesis testing with the ability to examine multiple alternative models against each other in a probabilistic manner. It returns the so-called model weights (Geman et al., 1992) representing posterior probabilities for each model to be the most appropriate one from the set of proposed competing models. Thus, the computed model weights provide a quantitative ranking for the competing conceptual models.

Let us consider N_m competing computational models M_k , each with an uncertain parameter vector θ_k of length N_k , yielding a quantity Q of interest in a physical space of x , y and z and for a time stamp of t . The model weights are given by Bayes’ theorem, which can be cast for a set of M_k competing models as

$$P(M_k|\mathcal{Y}) = \frac{p(\mathcal{Y}|M_k)P(M_k)}{\sum_{i=1}^{N_m} p(\mathcal{Y}|M_i)P(M_i)}, \quad (18)$$

where $P(M_k)$ denotes the prior probability of the model, also known as the subjective credibility that model M_k could be the the most plausible model in the set of models *before* any comparison with observed data have been made. The term $p(\mathcal{Y}|M_k)$ is the Bayesian model evidence (BME), also known as marginal likelihood, of the model M_k . Bayes' theorem closely follows the principle of parsimony or Occam's razor (Angluin & Smith, 1983), in that the posterior model weights $P(M_k|\mathcal{Y})$ offer a compromise between model complexity and goodness of fit, known as the bias-variance trade-off (Geman et al., 1992). The model weights, $P(M_k|\mathcal{Y})$, can be interpreted as the Bayesian probability of the individual models to be the best representation of the system from the pool of competing models.

Hoeting et al. (1999) propose that a 'reasonable, neutral choice' could be equally likely priors, i.e., $P(M_k) = 1/N_m$, in case of paucity of prior knowledge regarding the merit of the different models under consideration. The denominator in Equation (18) is the normalizing constant of the posterior distribution of the models and can simply be obtained by determination of the individual weights. Since all model weights are normalized by the same constant, this normalizing factor could even be neglected. Thus, the weights $P(M_k|\mathcal{Y})$ of the individual model M_k against other models can be represented by the proportionality

$$P(M_k|\mathcal{Y}) \propto p(\mathcal{Y}|M_k)P(M_k). \quad (19)$$

The BME term $p(\mathcal{Y}|M_k)$ quantifies the likelihood of the observed data based on the prior distribution of the parameters. It can be computed by integrating the likelihood term in Bayesian theorem (Kass & Raftery, 1995) over the parameter space Θ_k of the model M_k :

$$p(\mathcal{Y}|M_k) = \int_{\Theta_k} p(\mathcal{Y}|M_k, \theta_k)P(\theta_k|M_k)d\theta_k, \quad (20)$$

with θ_k being the parameter vector from the parameter space Θ_k of model M_k . The term $P(\theta_k|M_k)$ is the corresponding prior distribution of parameters θ_k for the model M_k . The likelihood or probability of the parameter set θ_k of model M_k to have generated the observation data with the independent realization of $\mathcal{Y} = (\mathcal{Y}_1, \dots, \mathcal{Y}_N)^T$ is represented by

$$\begin{aligned} p(\mathcal{Y}|M_k, \theta_k) &:= \prod_{i=1}^N p(\mathcal{Y}_i|M_k, \theta_k) \\ &= \frac{1}{\sqrt{(2\pi)^N \det \Sigma}} \exp \left(-\frac{1}{2} (M_k(\theta_k) - \mathcal{Y})^T \Sigma^{-1} (M_k(\theta_k) - \mathcal{Y}) \right), \end{aligned} \quad (21)$$

where Σ denotes the covariance matrix, which includes the all error sources to be explained in Section 4.2. To obtain the BME values for each competing models, we estimate the integral in (20) using a brute-force Monte Carlo integration (Smith & Gelfand, 1992) avoiding unnecessary assumptions. For more details on the properties of BME and a comparison of various techniques to estimate this term, the reader is referred to Schöniger et al. (2014) and Oladyshkin and Nowak (2019).

The ratio of BME values for two alternative models is defined as the Bayes Factor $BF(M_k, M_l)$, which is a key component in Bayesian hypothesis testing framework introduced in (Jeffreys, 1961):

$$BF(M_k, M_l) = \frac{P(M_k|\mathcal{Y})}{P(M_l|\mathcal{Y})} \frac{P(M_l)}{P(M_k)} = \frac{p(\mathcal{Y}|M_k)}{p(\mathcal{Y}|M_l)}. \quad (22)$$

It quantifies the evidence (literally, as in Bayesian model evidence) of the hypothesis M_k against the null-hypothesis M_l . Stated differently, the Bayes factor $BF(M_k, M_l)$,

Table 1. Interpretation of Bayes Factor in favor of model M_k according to (Jeffreys, 1961).

Bayes Factor (BF)	Interpretation
1 – 3	anecdotal evidence
3 – 10	substantial evidence
10 – 100	strong evidence
> 100	decisive evidence

can be interpreted as the ratio between the posterior and prior odds of model M_k being the more plausible one in comparison to the alternative model M_l (Kass & Raftery, 1995). Jeffreys (1961) provides a rule of thumb for the interpretation of Bayes factor. The grades of evidence are summarized in Table 1. Following this suggestion, a Bayes factor which lies between 1 and 3 indicates an evidence in favor of M_k that is ‘not worth more than a bare mention’, a factor of up to 10 represents ‘substantial’ evidence, and a factor between 10 and 100 can be regarded a ‘strong’ evidence. Finally, a Bayes factor greater than 100 admits ‘decisive’ evidence, i.e., it can be used as a threshold to reject models based on poor performance in comparison to the best performing model in the set of considered models.

3.2 Accelerating the Analysis via Surrogate Modeling

As stated earlier, BVF requires uncertainty propagation through each competing model, demanding a significant number of model evaluations to yield statistical convergence. In practice, however, the computational complexity of the underlying computational models and the total available computational budget severely restrict the number of evaluations that one can carry out. In such situations, the Bayesian analysis estimations lack sufficient trust as the limited number of model evaluations can yield additional uncertainty. To tackle this challenge, we replace each competing model’s response in the Bayesian validation framework with an easy-to-evaluate surrogate representation using the theory of PCE introduced in Wiener (1938).

The PCE representation of the model M_k provides the dependence of the computational model M_k on the uncertain model’s parameters θ_k using projection onto an orthonormal polynomial basis (Oladyshkin & Nowak, 2018). It could be also seen as a linear regression that includes linear combinations of a fixed set of nonlinear functions with respect to the input variables, known as polynomial basis function

$$M_k(x, y, z, t, \theta_k) \approx \sum_{\alpha \in \mathcal{A}} c_{\alpha}(x, y, z, t) \Psi_{\alpha}(\theta_k). \quad (23)$$

Here, x, y, z, t are the spatial and temporal components of the quantity of interest, θ_k is the vector of the N_k uncertain parameters of model M_k , $c_{\alpha}(x, y, z, t) \in \mathbb{R}$ are the corresponding expansion coefficients that are functions of space and time, and $\Psi_{\alpha}(\theta_k)$ represents multivariate polynomials orthogonal with respect to a multi-index α . The latter represents the combinatoric information how to enumerate all possible products of N_k individual univariate basis functions with respect to the total degree of expansions less or equal to polynomial degree d (Marelli et al., 2021):

$$\mathcal{A}^{N_k, d} = \{\alpha \in \mathbb{N}^{N_k} : |\alpha| \leq d\}, \quad \text{card } \mathcal{A}^{N_k, d} \equiv P = \binom{N_k + d}{d}. \quad (24)$$

The multivariate polynomials $\Psi_{\alpha}(\theta_k)$ are comprised of the tensor product of univariate polynomials

$$\Psi_{\alpha}(\theta_k) := \prod_{i=1}^{N_k} \psi_{\alpha_i}^{(i)}(\theta_{k,i}), \quad (25)$$

where the univariate orthonormal polynomials $\psi_{\alpha_i}^{(i)}(\theta_{k,i})$ must satisfy

$$\langle \psi_j^{(i)}(\theta_{k,i}), \psi_l^{(i)}(\theta_{k,i}) \rangle := \int_{\Theta_{k,i}} \psi_j^{(i)}(\theta_{k,i}) \psi_l^{(i)}(\theta_{k,i}) f_{\Theta_{k,i}}(\theta_{k,i}) d\theta_{k,i} = \delta_{jl}. \quad (26)$$

Here, i represents the input variable with respect to which the polynomials are orthogonal as well as the corresponding polynomial family, j and l are the corresponding polynomial degree, $f_{\Theta_{k,i}}(\theta_{k,i})$ is the i th-input marginal distribution and δ_{jl} is the Kronecker delta. We use an arbitrary polynomial chaos expansion (aPCE), introduced by Oladyshkin and Nowak (2012), that can operate with probability measures that may be implicitly and incompletely defined via their statistical moments. Using aPCE, one can build the multivariate orthonormal polynomials even in the absence of the exact probability density function $f_{\Theta_k}(\theta)$.

The main task of the surrogate representation of model $M_k(x, y, z, t, \theta_k)$ in Equation (23) is to compute the coefficients \mathbf{c}_α . However, not all coefficients could be relevant for such a surrogate. Therefore, we employ the Bayesian sparse learning method (Tipping, 2001) using a fast marginal likelihood maximization algorithm (Tipping & Faul, 2003). Doing so, we sequentially identify the relevant predictors (expansion terms) that capture the most significant features of the physical model. We denote this extension of aPCE as Bayesian sparse arbitrary polynomial chaos (BsaPCE) representation (Mohammadi, 2020). The posterior distribution of the expansion coefficients, conditioned on the model responses \mathbf{Y} resulting from the training sets \mathbf{X} , is given by the combination of a Gaussian likelihood and a Gaussian prior distribution over the unknown expansion coefficients \mathbf{c} according to Bayes' rule. Then, the posterior of the expansion coefficients given the model responses \mathbf{Y} and values of hyper-parameters α and β describing the Gauss process (Oladyshkin et al., 2020), can take the following form

$$p(\mathbf{c}|\mathbf{Y}, \alpha, \beta) = \frac{p(\mathbf{Y}|\mathbf{X}, \mathbf{c}, \beta)p(\mathbf{c}|\alpha)}{p(\mathbf{Y}|\mathbf{X}, \alpha, \beta)}, \quad (27)$$

which is also Gaussian defined by $\mathcal{N}(\mathbf{c}|\boldsymbol{\mu}, \boldsymbol{\Sigma})$ with

$$\boldsymbol{\mu} = \beta \boldsymbol{\Sigma} \boldsymbol{\Psi}^\top \mathbf{Y}, \quad \boldsymbol{\Sigma} = (\mathbf{A} + \boldsymbol{\Psi}^\top \beta \boldsymbol{\Psi})^{-1}. \quad (28)$$

Here, $\boldsymbol{\Psi}$ is the design matrix of size $E \times N$ with elements $\Psi_{ni} = \psi_i(x_n)$, where E represents the number of model evaluations using the training samples, and $\mathbf{A} = \text{diag}(\alpha_i)$. The values of α and β can be determined via type-II maximum likelihood (Berger, 2013). Having found values α^* and β^* for the hyperparameters that maximize the marginal likelihood, one can evaluate the predictive distribution over \mathbf{Y} for a new input \mathbf{x} by

$$\begin{aligned} p(\mathbf{Y}|\mathbf{x}, \mathbf{X}, \mathbf{Y}, \alpha^*, \beta^*) &= \int p(\mathbf{Y}|\mathbf{x}, \mathbf{c}, \beta^*) p(\mathbf{c}|\mathbf{X}, \mathbf{Y}, \alpha^*, \beta^*) d\mathbf{c} \\ &= \mathcal{N}(\mathbf{Y}|\boldsymbol{\mu}^\top \boldsymbol{\Psi}(\mathbf{x}), \sigma^2(\mathbf{x})). \end{aligned} \quad (29)$$

The predictive mean is given by (28) with \mathbf{c} set to the posterior mean $\boldsymbol{\mu}$, and the variance of the predictive distribution is given by

$$\sigma^2(\mathbf{x}) = (\beta^*)^{-1} + \boldsymbol{\Psi}(\mathbf{x})^\top \boldsymbol{\Sigma} \boldsymbol{\Psi}(\mathbf{x}), \quad (30)$$

where $\boldsymbol{\Sigma}$ is calculated by Equation (28) in which α and β set to their optimized values α^* and β^* . For the latter, a separate hyperparameter α_i is assigned to each weight parameter c_i .

4 Benchmark Scenario

Corresponding to Figures 1 and 4, we investigate rectangular solid inclusions of size d and consider a flow problem where the flow is arbitrary to the fluid-porous

interface Γ . We consider laminar fluid flow through the coupled flow domain and take the viscosity $\mu = 10^{-3}$. We describe the geometrical configuration and the boundary conditions in Section 4.1, followed by a description of the uncertainties in Section 4.2 and the system response quantities in Section 4.3.

4.1 Geometrical Setting and Boundary Conditions

We consider the free-flow region $\Omega_{\text{ff}} = (0, L) \times (\gamma, H)$ and the porous-medium domain $\Omega_{\text{pm}} = (0, L) \times (0, \gamma)$ with $L = 10.25$ mm and $H = 6$ mm, separated by the sharp fluid–porous interface Γ , where the exact value for γ is uncertain. The porous medium is isotropic, $\mathbf{K} = k\mathbf{I}$, and consists of 20×10 square solid inclusions of size $d = 0.25$ mm (Figure 4) leading to porosity $\phi = 0.75$. The inclusions are positioned in such a way that the line tangent to the top of the upper row of solid inclusions is given by $(0, L) \times \{5 \text{ mm}\}$ and the characteristic pore size appearing in coupling condition (12) is $\ell = 0.5$ mm.

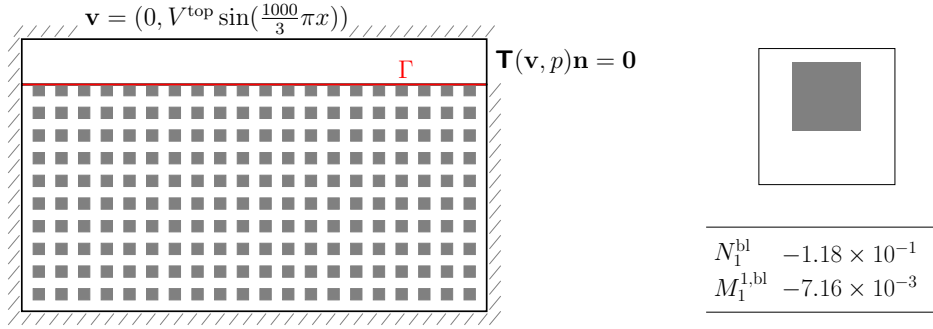


Figure 4. Schematic description of the coupled flow problem (left) and non-dimensional effective properties for the interface location $\gamma = 5.05$ mm (right).

For the classical interface conditions (7)–(9) (*Classical IC*) the Beavers–Joseph parameter is typically taken $\alpha_{\text{BJ}} = 1$ in the literature, although it is often not the optimal choice (Rybak et al., 2021; Mierzwiczak et al., 2019; Lācis et al., 2020). Here, we consider α_{BJ} as an uncertain parameter, which is quantified in Sections 4.2 and 4.3. The boundary layer constants appearing in the generalized coupling conditions (10)–(12) (*Generalized IC*) are computed numerically based on the geometrical configuration of the interfacial zone and are presented in Figure 4 (right). For details on the computation of these effective parameters, we refer the reader to (Eggenweiler & Rybak, 2021). Note that the boundary layer constants N_1^{bl} and M_1^{bl} (Figure 4, right) are non-dimensional. For isotropic porous media, the constants $M_1^{2, \text{bl}} = 0$ and $N_s^{\text{bl}} = 0$, therefore, they do not appear in Figure 4 (right).

In order to obtain a closed formulation for the pore-scale problem (1)–(2) we set the following boundary conditions on the external boundary

$$\mathbf{v} = \mathbf{v}_{\text{in}} = (0, V^{\text{top}} \sin(\frac{1000}{3} \pi x)) \quad \text{on } \Gamma_{\text{in}}, \quad (31)$$

$$\mathbf{T}(\mathbf{v}, p)\mathbf{n}_{\text{ff}} = 0 \quad \text{on } \Gamma_{\text{out}}, \quad (32)$$

$$\mathbf{v} = 0 \quad \text{on } \Gamma_{\text{nf}}, \quad (33)$$

where the inflow boundary $\Gamma_{\text{in}} = (3 \text{ mm}, 6 \text{ mm}) \times \{H\}$, $\Gamma_{\text{out}} = \{L\} \times (5.5 \text{ mm}, H)$, $\Gamma_{\text{nf}} = \partial\Omega \setminus (\Gamma_{\text{in}} \cup \Gamma_{\text{out}})$ and \mathbf{n}_{ff} is the outward unit normal vector on $\partial\Omega_{\text{ff}}$. The boundary conditions for the coupled flow problem are presented schematically in Figure 4 (left).

The corresponding boundary conditions for the REV-scale model formulation given by (3)–(4) together with either the *Classical IC* (7)–(9) or the *Generalized IC* (10)–(12), which are valid for arbitrary flow directions, read

$$\mathbf{v}_{\text{ff}} = (0, V^{\text{top}} \sin(\frac{1000}{3}\pi x)) \quad \text{on } \Gamma_{\text{in}}, \quad (34)$$

$$\mathbf{T}(\mathbf{v}_{\text{ff}}, p_{\text{ff}}) \mathbf{n}_{\text{ff}} = \mathbf{0} \quad \text{on } \Gamma_{\text{out}}, \quad (35)$$

$$\mathbf{v}_{\text{ff}} = \mathbf{0} \quad \text{on } \Gamma_{\text{nf,ff}}, \quad (36)$$

$$\mathbf{v}_{\text{pm}} \cdot \mathbf{n}_{\text{pm}} = 0 \quad \text{on } \Gamma_{\text{nf,pm}}, \quad (37)$$

where $\Gamma_{\text{nf,ff}} = \partial\Omega_{\text{ff}} \setminus (\Gamma_{\text{in}} \cup \Gamma_{\text{out}} \cup \Gamma)$, $\Gamma_{\text{nf,pm}} = \partial\Omega_{\text{pm}} \setminus \Gamma$ and \mathbf{n}_{pm} denotes the unit normal vector on $\partial\Omega_{\text{pm}}$ pointing outward the porous medium.

The boundary conditions (34)–(36) also hold for the hybrid-dimensional free-flow/pore-network model (*Pore-Network model*), such that no mass enters or leaves the domain through the pores on $\Gamma_{\text{nf,pm}}$. The coupling conditions (13)–(15) are set on Γ for PNM.

4.2 Uncertainties and Errors

So far, we have presented various coupling concepts for free flow and porous-medium flow. These concepts differ in the description of processes in the porous region and across the fluid–porous interface, where different mathematical models are employed, whereas the free flow for all concepts is modeled based on the stationary Stokes equations. The uncertainty, due to the choice of adequate representation of the system of interest, is known as conceptual uncertainty. In addition to the conceptual uncertainty, each computational model includes uncertain parameters, such as material parameters, or interface location, requiring a thorough investigation. This type of uncertainty is known as parametric uncertainty. Uncertain model inputs, defined later, must be propagated through the model or simulation (also known as uncertainty propagation) to effectively assess competing modeling concepts’ response quantities and validate the corresponding computational models against a reference solution.

Regarding the coupled Stokes–Darcy model with the *Classical IC*, the benchmark scenario contains four uncertain parameters: the maximum boundary velocity at the inflow boundary, the exact interface position, the Beavers–Joseph coefficient, and the permeability tensor. We refer to Section 1 for a brief literature overview on the role of these model parameters. In contrast to the *Classical IC*, the *Generalized IC* do not contain the Beavers–Joseph coefficient. Further, the *Generalized IC* rely on the assumption that the interface location may not be below the top of the solid inclusions. Correspondingly, the parameters and their associated distributions as prior knowledge for the Stokes–Darcy model with the *Classical IC* and the *Generalized IC* are listed in Table 2 and Table 3, respectively.

Table 2. The uncertain parameters and their defined distributions for the classical coupled Stokes–Darcy model.

Parameter name	Range	Unit	Distribution type
Boundary velocity, V^{top}	$[5 \times 10^{-4}, 1.5 \times 10^{-3}]$	m/s	uniform
Exact interface location, Γ	$[4.9, 5.1]$	mm	uniform
Permeability, k	$[10^{-10}, 10^{-8}]$	m ²	log normal
Beavers–Joseph parameter, α_{BJ}	$[0.1, 4]$	-	uniform

Table 3. The uncertain parameters and their associated distributions for the Stokes–Darcy model with the generalized interface conditions.

Parameter name	Range	Unit	Distribution type
Boundary velocity, V^{top}	$[5 \times 10^{-4}, 1.5 \times 10^{-3}]$	m/s	uniform
Exact interface location, Γ	$[5.0, 5.1]$	mm	uniform
Permeability, k	$[10^{-10}, 10^{-8}]$	m ²	log normal

As for the *Pore-Network* model, we consider the total conductance g_{ij} in (6) (see Figure 2) as uncertain parameter to be inferred during the calibration phase. This parameter plays the role of permeability in the pore-network setting. Another uncertain input parameter is the pore-scale slip coefficient β_{pore} . It can be determined numerically in a preprocessing step, in which it is approximated by solving a simplified, equivalent problem of free flow over a single pore throat intersecting with the lower boundary of the free-flow channel (Weishaupt et al., 2020). The list of considered uncertain parameters and their associated distribution as prior knowledge for the PNM model are presented in Table 4.

Table 4. The uncertain parameters and their specifications for the pore-network model.

Parameter name	Range	Unit	Distribution type
Boundary velocity, V^{top}	$[5 \times 10^{-4}, 1.5 \times 10^{-3}]$	m/s	uniform
Total conductance, g_{ij}	$[10^{-7}, 10^{-5}]$	m ³ /(s · Pa)	uniform
Pore-local slip coefficient, β_{pore}	$[10^3, 10^5]$	1/m	uniform

As opposed to uncertainties, errors are defined as the difference between the true value and the predicted value, and have both a sign and a magnitude. We consider the errors associated with the model discrepancy error, numerical approximation, and surrogate modeling in our analysis. These errors are aggregated and used as diagonal entries of the residual covariance matrix Σ in the likelihood function in Equation (21).

Model discrepancy error. In the current benchmark case study, we have a fully resolved pore-scale solution as a reference. However, in practice, the reference solution is not available, and instead, experimental data is incorporated that includes an observation error. Nevertheless, the analyzed models in our benchmark study could never perfectly reproduce the ground truth, i.e., the reference solution. This difference can be attributed to the presence of model discrepancy. This discrepancy always exists for various reasons, such as simplified assumptions, missing physics, upscaling due to scale differences. Several methods have been proposed in the literature to incorporate the model discrepancy in a Bayesian setting. These methods’ treatment of model discrepancy range from a constant bias to more sophisticated methods in which one forms a Bayesian hierarchical model to solve a joint parameter and model discrepancy inference problem (Kennedy & O’Hagan, 2001; Bayarri et al., 2007; Brynjarsdóttir & O’Hagan, 2014; Ling et al., 2014; Gardner et al., 2021). Since the model discrepancy is not perfectly known, we parametrize it, i.e., $\Sigma(\theta_\epsilon)$ and treat its parameter θ_ϵ as additional unknown parameters. Following Wagner et al. (2021), we infer these parameters jointly with model parameters θ_k in Equation (21). We consider a diagonal covariance matrix as $\Sigma = \sigma^2 \mathbb{I}_{N_{\text{out}}}$ with a scalar unknown parameter σ^2 for each system response quantity, i.e., velocity and pressure (Section 4.3).

Numerical error. The governing equations of the models under investigation in this study require approximation of numerical solutions. These approximations provide an additional source of error. There are five primary sources of errors in computational physics solutions, given that the numerical scheme is stable, consistent, and robust. These sources are insufficient spatial discretization, insufficient temporal discretization, insufficient iterative convergence, computer round-off, and computer programming (Roy, 2019). Since quantifying errors from these sources is the main focus in the verification of numerical schemes, we only investigate the discretization error that originates from a certain choice of mesh size. Following Oberkampf and Roy (2010), we take a heuristic approach to quantify this error, in that we fit generalized Richardson extrapolation to estimate the error by comparing three different mesh spacings. The Richardson extrapolation takes the following form

$$f_k = \bar{f} + e_p h_k^{\hat{p}} + \mathcal{O}(h_k^{\hat{p}+1}), \quad (38)$$

where f_k denotes the exact solution to the discrete equation on a mesh with a known spacing h_k , \bar{f} stands for the exact solution to the original PDE (unknown). e_p is the error term coefficient, and \hat{p} indicates the observed order of accuracy. Here, we seek the first-order error. Thus, the unknowns \bar{f} and e_p can be easily determined via the least square method for the numerical solutions obtained by varying the mesh spacing.

Surrogate error. As previously mentioned, we substitute the computational models with the easy-to-evaluate surrogate models in the Bayesian analysis to offset the computational cost. This replacement also introduces a new source of error, known as a surrogate prediction error. Ignoring this error could result in a biased posterior distribution. As for prediction uncertainty, a mean squared error based on a testing set can provide a good estimate of the surrogate error variance.

We incorporate the errors discussed above in the Markov Chain Monte Carlo (MCMC) simulation method to approximate the posterior distribution (Robert & Casella, 2013; Liu, 2008), used in the calibration stage. We directly sum up all the covariance matrices of errors to obtain the likelihood calculations' total covariance matrix. Here, we assume that all these errors follow a normal distribution and are independent of each other.

4.3 System Response Quantities

A fundamental ingredient of each benchmark is the definition of so-called system response quantities (SRQs). These quantities define the prescribed output from the reference/experimental data as well as from the computational models that are compared in terms of the validation metric. The SRQs can be either local or global quantities. While the former can take quantities within the solution domain on the PDEs, such as dependent variables of the PDEs, the latter represents integral quantities or net flux out of a system. As part of model validation, we seek to compare system responses generated by different coupling concepts with the ones from the pore-scale resolved model (Section 2.1). Figure 5 shows the data extraction points for the velocity field (left) and the pressure (right). We train the surrogate models for all computational models based on the simulation results for the marked points. The points colored in blue and red provide the corresponding data for the calibration and validation steps, respectively.

The pore-scale resolved simulation results contain both macroscopic and microscopic details of the flow field. The latter become visible as oscillations of the pore-scale solutions in the porous medium. To make numerical simulation results comparable we need to average them at the pore and REV scale. We consider volume averaging,

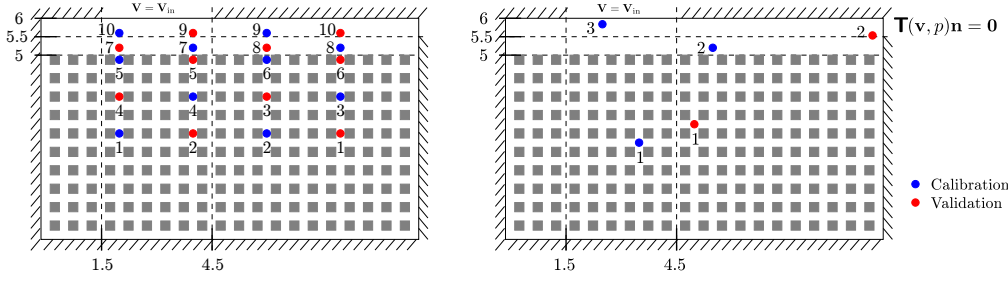


Figure 5. Data extraction points for the velocity field (left) and pressure (right) for the calibration and validation scenarios.

where the averaged velocity field at a given point $\mathbf{x}_0 \in \Omega$ is obtained as

$$\mathbf{v}_{\text{avg}}(\mathbf{x}_0) = \frac{1}{|V(\mathbf{x}_0)|} \int_{V_f(\mathbf{x}_0)} \mathbf{v}(\mathbf{x}) \, d\mathbf{x}, \quad (39)$$

where $V(\mathbf{x}_0)$ is the representative elementary volume corresponding to \mathbf{x}_0 and $V_f(\mathbf{x}_0)$ is its fluid part. The representative elementary volume $V(\mathbf{x}_0)$ has the same size as the periodicity cell Y^ℓ . Moreover, also the simulation results in the free-flow region need to be averaged correspondingly such that the interpretation of the SRQs is the same in all cases.

5 Application of the Bayesian Framework

In this section, we compare the coupled models (using either REV-scale formulation or *Pore-Network* model in Ω_{pm}) with the pore-scale resolved model (1)–(2). For the REV-scale model formulation, we consider the Stokes–Darcy problem with the *Classical IC* (7)–(9) and the *Generalized IC* (10)–(12). We demonstrate that the latter ones are more accurate than the *Classical IC* in case of parallel flows to the interface and that they are suitable for arbitrary flow directions where the *Classical IC* fail. As shown in Weishaupt et al. (2019, 2020), the hybrid-dimensional coupled model using a *Pore-Network* approach in Ω_{pm} can be an efficient and accurate choice for simulating free flow over structured porous media.

Here, our goal is to assess the coupled model’s accuracy in comparison to the above-mentioned REV-scale approaches and under the influence of pore-scale parameter uncertainty. As a reference data we use the fully resolved pore-scale model for the velocity and pressure (Figure 6). However, it is worth mentioning that the Stokes–Darcy model with *Classical IC* and *Generalized IC* can only offer predictions on the REV scale. Therefore, we average the values of SRQs obtained for the fully resolved pore-scale model and as well as the *Pore-Network* model for consistency. The averaging is performed via a volume averaging approach, discussed in Section 4.3 to make the REV-scale numerical simulation results comparable with that of the pore-scale resolved simulation.

The pore-scale model and the coupled models have been implemented in the open-source simulator DuMu^x (Koch, Gläser, et al., 2021). The Bayesian analysis has been performed using a new open-source, object-oriented Python framework *BayesValidRox*. This framework provides an automated workflow for surrogate-based sensitivity analysis, Bayesian calibration, and validation of computational models with a modular structure.

Replacing the models with their surrogates drastically reduces the total computational time of the analysis. This gain is essential in computationally demanding

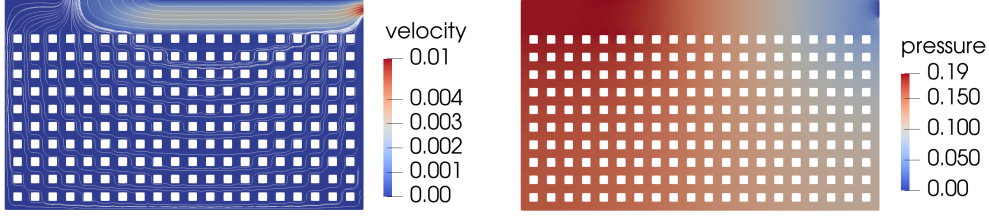


Figure 6. Streamlines of the pore-scale velocity field (left) and the pressure (right).

uncertainty quantification tasks, such as propagation or inference. In this study, we observed that by using a well-trained surrogate model, we could speed up one simulation run from 10 ~ 15 s to only 0.005 ~ 0.007 s with acceptable accuracy.

The current section offers insights into analysis of predictive abilities in Section 5.2 and model comparison in Section 5.3 using the surrogate-based Bayesian validation framework introduced in Section 3. Additionally, we assess the influence of various modeling parameters onto the final model prediction, performing the global sensitivity analysis in Section 5.1.

5.1 Global Sensitivity Analysis

In this section, we analyze how the variability of the model response quantities, introduced in Section 4.3, at the selected data extraction points (Figure 5), is affected by the variability of each input variable or combinations thereof. This is achieved via a sensitivity analysis. Various sensitivity analysis approaches have been developed in the recent years. For an extensive review of different techniques, see (Iooss & Lemaître, 2015). In the current paper, we explore the connection of polynomial representation to a global sensitivity measures (Oladyshkin et al., 2012) and use the so-called *Sobol' indices* (Sobol', 1993), derived from a variance decomposition of model outputs in terms of contributions of each input parameter or combinations thereof. Using Sobol' decomposition, one can describe the total variance of the model in terms of the sum of the summands' variances. This variance decomposition is extensively explained in (Sudret, 2008). Leveraging the orthonormality of the polynomial chaos basis, the authors also derive so-called PC-based Sobol' indices. The idea behind these indices is as follows: once the PC representation of the model in (23) is available, the expansion coefficients c_α are simply gathered according to the dependency of each basis polynomial, square-summed and normalized

$$S_{i_1, \dots, i_s} = \frac{\sum_{j=1}^M \chi_j c_j^2}{\sum_{j=1}^M c_j^2}, \quad \chi_j = \begin{cases} 1, & \text{if } \alpha_j^k > 0, \quad \forall j \in (i_1, \dots, i_s) \\ 0, & \text{if } \alpha_j^k = 0, \quad \exists j \in (i_1, \dots, i_s) \end{cases}. \quad (40)$$

Here, S_{i_1, \dots, i_s} is the Sobol' index that indicates what fraction of total variance of the response quantity can be traced back to the joint contributions of the parameters $\theta_{i_1}, \dots, \theta_{i_s}$. The index selection operator χ_j indicates where the chosen parameters θ numbered as i_1, \dots, i_s (i.e., $\theta_{i_1}, \dots, \theta_{i_s}$) have concurrent contributions to the variance within the overall expansion. Simply put, it selects all polynomial terms with the specified combination i_1, \dots, i_s of model parameters.

A complementing measure for sensitivity analysis is the *Sobol' Total Index*. It expresses the total contribution to the variance of model output due to the uncertainty of an individual parameter θ_j in all cross-combinations with other parameters

$$S_j^T = \sum_{\{i_1, \dots, i_s\} \supset j} S_{i_1, \dots, i_s}, \quad (41)$$

where S_j^T is simply a summation of all Sobol indices in which the variable θ_j appears as univariate as well as joint influences. The Total Sobol indices sum to one, if input variables are independent. When dealing with correlated variables, however, this is not the case. In what follows, we present the total Sobol indices for the SQRs and the data extraction points defined in Section 4, for all three models for the validation scenario.

Classical IC. In Figure 7, we provide the total Sobol indices for the validation points in blue (Figure 5) for velocity and pressure. We observe that the boundary velocity V^{top} has the most contribution to the velocity variance (Figure 7, left) in the free-flow region and pressure field (Figure 7, right) for the analyzed points in the domain. Moreover, the exact interface location plays an important role for the velocity field, especially near the interface (Figure 7, left) and influences the pressure field as well (Figure 7, right). The value of the Beavers–Joseph parameter has a higher impact on the velocity near the interface than other parts of the domain. However, this parameter does not play an essential role for the pressure. The permeability k significantly affects the velocity in the porous-medium domain, whereas its influence on the velocity in the free-flow region and the pressure field is small.

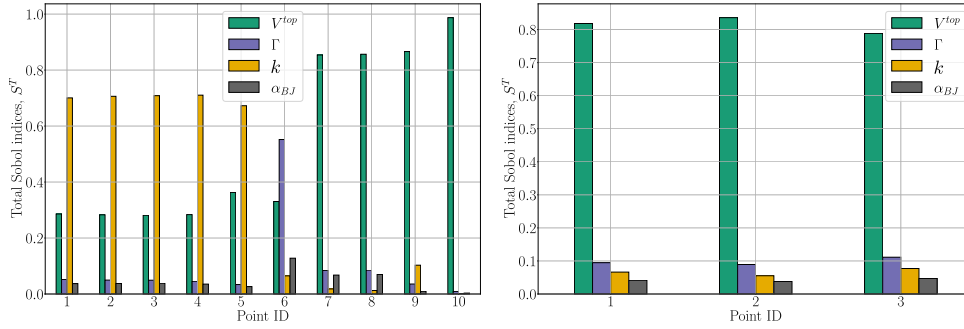


Figure 7. Total Sobol indices of the Stokes–Darcy model with the *Classical IC* for the velocity (left) and pressure (right) for the calibration (blue) points in Figure 5.

Generalized IC. In Figure 8, the total Sobol indices for velocity and pressure before calibration are presented for the selected blue points in Figure 5. For the *Generalized IC*, the information about the exact interface location Γ is included in the boundary layer constants N_1^{bl} and $M_1^{1,\text{bl}}$ appearing in condition (12). Therefore, the exact position of interface does not influence the overall system behavior in comparison to the *Classical IC*. The permeability k and the inflow velocity V^{top} have significant impact both on the velocity (in the free-flow region) and the pressure field, as in the case of the *Classical IC*.

Pore-network model. Figure 9 shows the total Sobol indices for velocity (left) and pressure (right) before calibration for the blue points in Figure 5. As for the REV-scale coupled models, we observe a dominant influence of V^{top} for all points. As expected, the influence of the total conductance is more prominent in the porous domain, which is comparable to the influence of permeability for the REV-scale coupled models. The influence of the pore-scale slip parameter β_{pore} shows a relatively small influence on the variability of velocity at point 6 and is hardly visible at other locations in the free-flow region. This matter is most likely because the slip coefficient only affects the flow field in the free-flow domain Ω_{ff} very locally, directly above the interface pore. The averaging volume used for the evaluation, however, takes into account a larger portion of the free-flow region, where the influence of β_{pore} is fairly small. In analogy

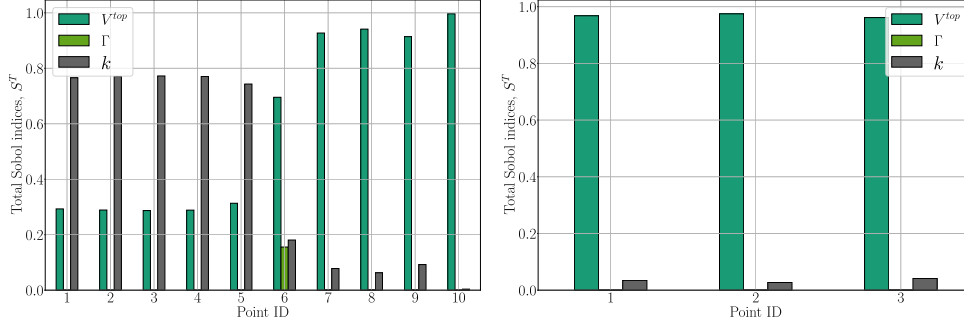


Figure 8. Total Sobol indices of the Stokes–Darcy model with the *Generalized IC* for the velocity (left) and pressure (right) for the calibration (blue) points in Figure 5.

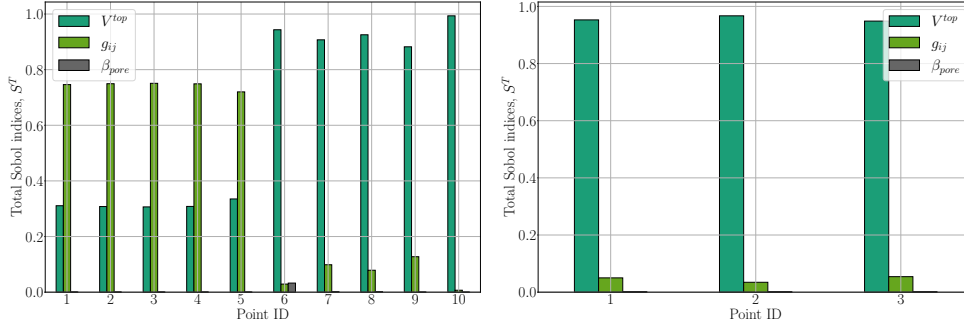


Figure 9. Total Sobol indices of the *Pore-Network* model for the velocity (left) and pressure (right) for the calibration (blue) points in Figure 5.

to the REV models, V^{top} also has a dominating influence on the pressure and velocity in the free-flow region.

5.2 Analysis of Predictive Abilities

In this section, we present the result of the analysis of the predictive ability of all three discussed conceptual models by showing their parametric posterior and the corresponding predictive distributions. These results are generated via the surrogate-based Bayesian procedure described in Section 3. In the calibration phase, we update the prior knowledge on the uncertain model parameters according to Section 4.2. We condition the responses of all analyzed models on the velocity and pressure values extracted from the pore-scale simulations that are marked as a blue points in Figure 5. To do so, we employ MCMC approach via *emcee* Python ensemble sampling toolkit (Foreman-Mackey et al., 2019) to perform Bayesian inference in Section 3.1 using BsaPCE surrogate representation in Section 3.2. We use an Affine Invariant Ensemble Sampler (AIES) to approximate the posterior distribution. For more details on MCMC, we refer the reader to (Goodman & Weare, 2010).

To accelerate this Bayesian updating step, we train each surrogate model with the simulation outcomes of 300 runs of each numerical model. The AIES-MCMC sampler is run for an ensemble of 50 Markov chains on each surrogate. We monitor the convergence of the sampler using the integrated auto-correlation time, which estimates the number of evaluations of the posterior probability density function to draw independent samples from the target density (Sokal, 1996). The MCMC sampler is run until the convergence criterion of 1% for the difference in the auto-correlation time

between two consequent monitoring steps is met. We retrain a new set of surrogate models in the validation stage based on the updated parameter distribution (posterior distribution) obtained after calibration. With these surrogate models, we propagate the posterior parametric uncertainty to estimate the posterior predictive distribution of models to be passed to the Bayesian metric calculation step.

As discussed in Section 4.2, using surrogates may introduce additional errors to the inference process. To include this error, we test the surrogate models with 150 simulation runs (test sets) which are different from the training sets. Comparing the surrogates' prediction with the results from the test sets, we observed a considerably low validation error between 10^{-8} and 10^{-11} for all models, indicating an acceptable prediction accuracy. Moreover, we estimated Mean Square Error (MSE) for each surrogate model that is a good estimate of the surrogate error variance (Xu & Valocchi, 2015). When evaluating the likelihood $p(\mathcal{Y}|M_k, \theta_k)$ in (21), we add a diagonal matrix $\Sigma_{\text{PCE},i}$ with elements $\sigma_{\text{PCE},i}^2 = \text{MSE}_i$, $i = 1, 2, \dots, N_{\text{out}}$ to Σ , assuming that the surrogate errors are independent and follow a normal distribution with zero mean. Moreover, following Schöniger et al. (2015), we perturb the reference data with some additive noise to account for uncertainty associated with the BME values, the resulting Bayes factors, and posterior model weights. With this approach, we investigate the impact of other possible sources of errors on the validation metrics that are not considered in the calculations.

As mentioned in Section 4.2, we jointly infer the uncertain parameters with the scalar unknown parameters σ_{vel}^2 and σ_p^2 for each system response quantity, i.e., velocity and pressure. For these parameters, we assume uniform distributions $\sigma_{vel}^2 \sim \mathcal{U}[0, 10^{-5}]$ and $\sigma_p^2 \sim \mathcal{U}[0, 10^{-3}]$ as priors, for velocity and pressure, respectively. In what follows, we present the updated (posterior) distribution of the parameters and model discrepancy errors after calibration obtained by the MCMC sampler for all three models. Afterward, a figure containing the posterior predictive of models next to each other versus the reference data is provided.

Classical IC. Figure 10 presents the posterior distribution obtained via the Bayesian inference using the calibration (blue) points in Figure 5. The 50 percent quantiles, alongside the 15 and 85 percent quantiles, are displayed on top of the histograms shown in the diagonal plots. The posterior follows a multivariate Gaussian distribution. Moreover, a slight correlation between the interface location Γ and the Beavers–Joseph parameter α_{BJ} is observed.

Generalized IC. Similar to the described procedure above, the surrogate-based Bayesian calibration offers insight into the posterior distributions of modeling parameters for the Stokes–Darcy model with the *Generalized IC* (Figure 11). The posterior distribution of uncertain parameters follows a multivariate Gaussian distribution. As opposed to the *Classical IC*, the interface location Γ for this interface condition shows a slightly wider distribution. This observation is in accordance with the findings in the sensitivity analysis, i.e., the exact position of interface does not influence the overall system behavior in comparison to the *Classical IC*.

Pore-network model. For the *Pore-Network* model, we also have used the calibration (blue) points (Figure 5) to perform surrogate-based Bayesian inference. Figure 12 illustrates the posterior parameter distribution of the *Pore-Network*. Similar to the *Classical IC* and *Generalized IC* models, we observe Gaussian shapes of posteriors. The distribution of β_{pore} covers a wider range. This issue can be attributed to insensitivity of the model results to this parameter, as presented by the total Sobol indices in Figure 9.

To obtain the models' posterior predictive distributions, we need to propagate the posterior parametric uncertainty presented so far through the models. The result

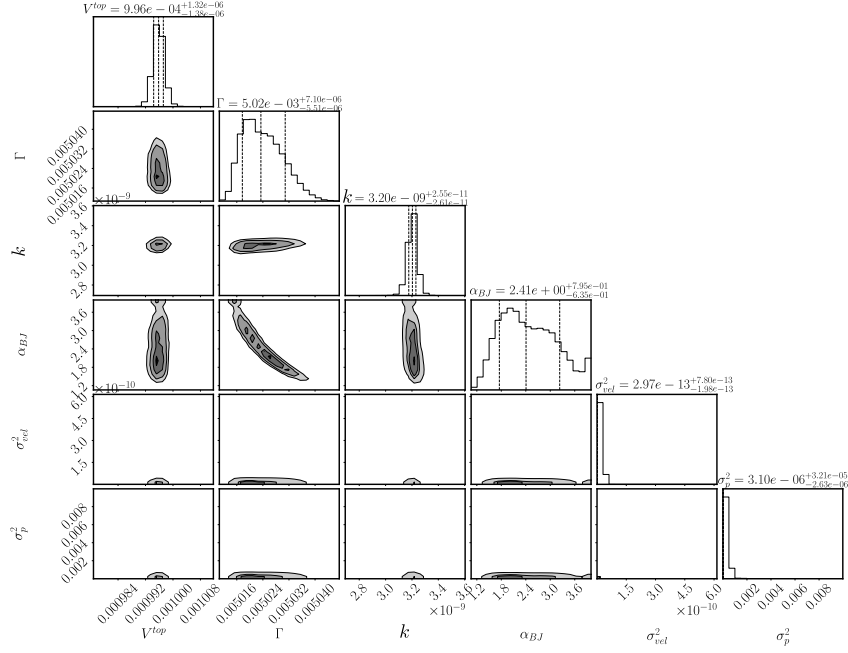


Figure 10. Posterior parameter distribution of the Stokes–Darcy model with the *Classical IC* after calibration to the reference data from the pore-scale model.

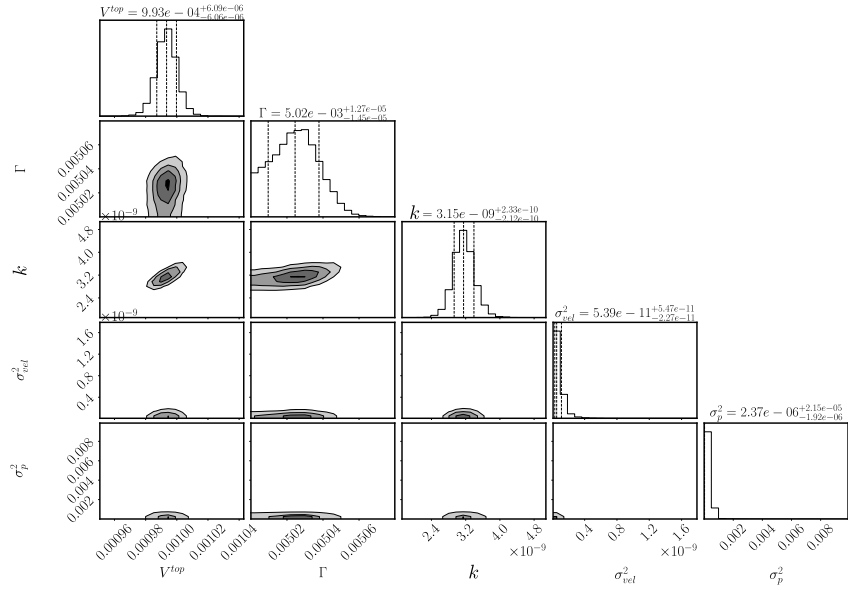


Figure 11. Posterior parameter distribution of the Stokes–Darcy model with the *Generalized IC* after calibration to the reference data from the pore-scale model.

offers a possibility of analyzing how post-calibration uncertainty affects the SRQs. To do so, we have trained a new set of surrogates using the information obtained during the calibration step. For better visual comparison, we plot the posterior predictive of models next to each other. Figures 13 and 14 illustrate the mean and standard deviations of the model predictive distributions in a bar chart for the velocity and pressure response quantities, respectively.

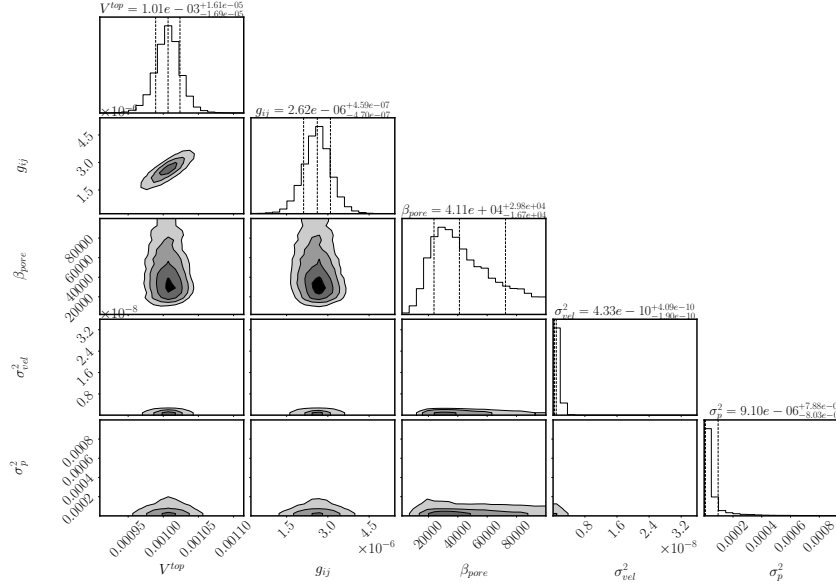


Figure 12. Posterior parameter distribution of the *Pore-Network* model after calibration to the reference data from the pore-scale model.

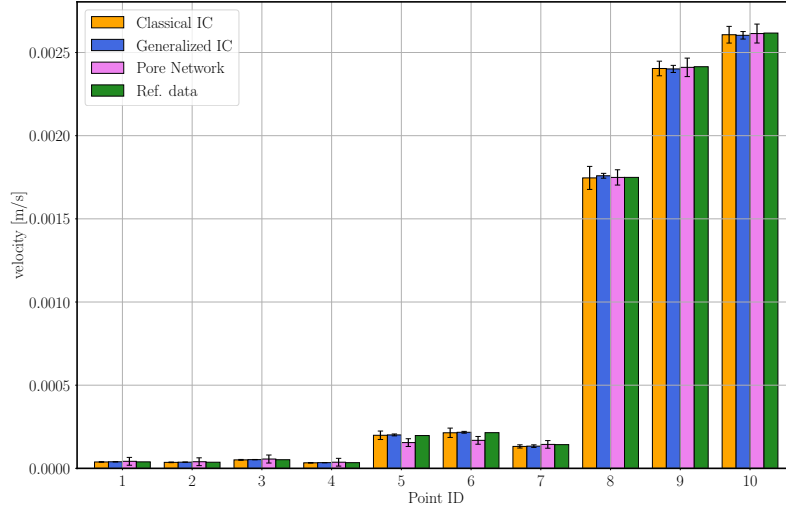


Figure 13. The velocity predictions of all models in the validation step against the reference data from the pore-scale model.

In particular, Figure 13 reveals that all analyzed models provide accurate predictions at the points located in the deeper part of the porous medium (1 to 4). However, the predictions at the points near the interface (5 to 8) suggest that the Stokes–Darcy model with *Classical IC* and *Generalized IC* provide more accurate predictions than the *Pore-Network* model. The REV-scale model with *Generalized IC* shows less uncertainty, i.e., lower standard deviation, in its prediction at the vicinity of the interface between the porous medium and the free-flow. Moreover, Figure 14 confirms that all models are able to provide accurate pressure values.

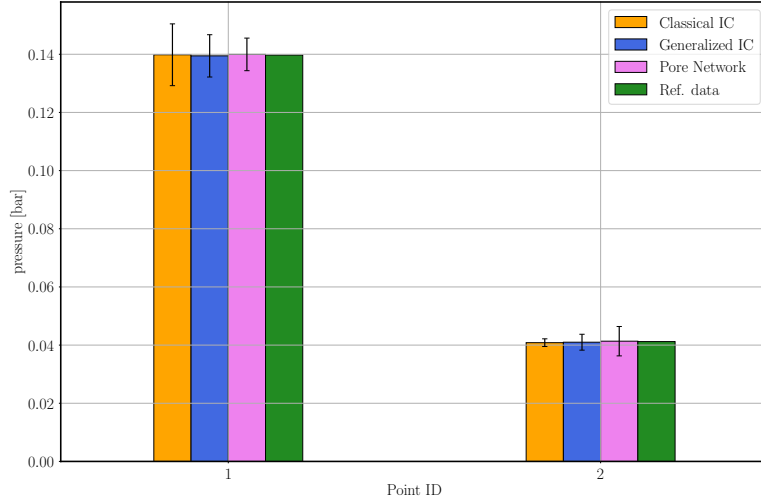


Figure 14. The pressure predictions of all models in the validation step against the reference data from the pore-scale model.

5.3 Model Comparison

We perform model comparison employing the so-called posterior model weights according to the Bayesian approach explained in Section 3.1. Such an analysis offers an aggregated comparison of a model’s outputs to the validation set of reference data from the pore-scale model that are marked in red in Figure 5. For model comparison analysis, we use the newly constructed surrogate representation during the validation stage to compute the BME values in (20). These values are required to calculate the posterior model weights (18) and the Bayes factors in (22). Additionally, use of the advanced surrogate representation provides a possibility to assess uncertainty of the BME values and the corresponding model weights. Table 5 presents a detailed statistical summary of the model weights and provides a ranking. It also reports the information regarding the post-calibration uncertainty with help of the deviation regarding 25% and 75% percentiles.

Table 5. The statistical summary of posterior model weights after validation.

Model	Model weights	Rank
Classical IC	$0.003^{+0.002}_{-0.001}$	2
Generalized IC	$0.997^{+0.001}_{-0.002}$	1
Pore-network	$0.000^{+0.000}_{-0.000}$	3

The expected model weights under noisy pore-scale data assumption convey a relatively clear model ranking in favor of *Generalized IC*, with *Classical IC* as second and the *Pore-Network* model ranking last. It is worth mentioning that the model weight close to zero for the *Pore-Network* model can be attributed to the high prediction uncertainty of this model. This fact is represented by the error bars in Figure 13. Moreover, a considerable mismatch can be detected between the expected velocity prediction of the *Pore-Network* model and the reference data at validation points 5

and 6. As for the *Classical IC*, the velocity prediction uncertainty is higher than that of the *Generalized IC*. This difference is mainly for the points at the vicinity of the interface and in the free-flow region.

Assessments of confidence in model ranking have been investigated by means of Bayes factor (22) for pairwise comparison of models based on the validation scenario. In the introduced uncertainty-aware Bayesian validation framework, Bayes Factors provide an objective measure of significance that quantifies the evidence in favor of one model's superiority against another. Figure 15 presents the probability density functions of $\log_{10}(\text{BF})$ over all perturbed velocity and pressure data sets in a three-by-three matrix. Here, we compute three Bayes factors for each model against its counterpart. The significant levels in a \log_{10} -scale, introduced in (Jeffreys, 1961) are marked with the vertical lines. Gray lines represent equally strong evidence for both models. Orange and red lines indicate thresholds for strong and decisive evidence in favor of one model against the other, respectively.

The first plot in the second row in Figure 15, e.g., shows the distribution of $\log_{10}(\text{BF})$ in favor of *Generalized IC* against *Classical IC*. This plot reveals that for most of the perturbed data sets, the Bayes factor is in the region where a decisive evidence ($\log_{10}(\text{BF})$ greater than two) exists in favor of *Generalized IC* to outperform *Classical IC*. Similarly, in all the analyzed cases (perturbed data sets), *Classical IC* could be clearly favored against *Pore-Network* model based on the decisive evidence (the plot in the first row, the last column). Moreover, the distribution in the second row, third column of Figure 15 reveals that the Bayes factor distribution of *Generalized IC* against *Pore-Network* model proves a decisive evidence in favor of *Generalized IC*.

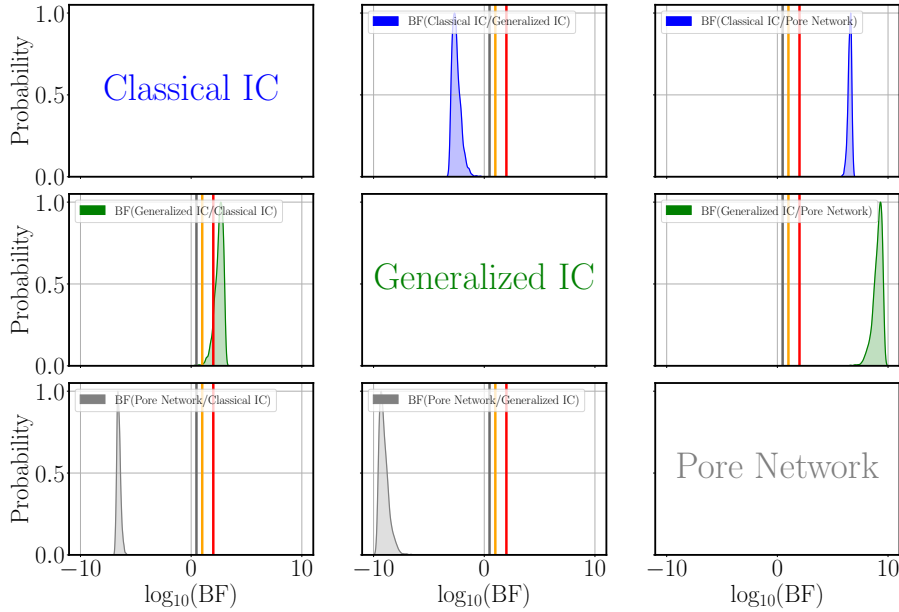


Figure 15. Distributions of \log_{10} (Bayes factor) for the pairwise comparison of competing models based on the validation scenario.

The results presented so far are based on a comparison of the SRQs with averaged SRQs of the fully resolved Stokes simulation, as the Stokes–Darcy model with *Classical IC* and *Generalized IC* could offer a prediction on the REV scale only. However, one could directly compare the *Pore-Network* model to the reference data at the pore scale without performing volume averaging by calculating the surface-averaged pore-

scale velocity at the pore-throat cross-sections. We denote the *Pore-Network* model with pore-throat surface averaging model as *Pore-Network SA* model and its Bayes factors distribution is shown in Figure 16. The velocities of *Pore-Network SA* model are not defined within the pore bodies but only at the pore throats, which explains why the results of Figure 16 show stronger evidence in favor of the *Pore-Network SA* model compared to the other concepts. Therefore, the original *Pore-Network SA* model avoiding additional averaging steps is a suitable approach when detailed pore-scale information is considered. Alternatively, the Stokes–Darcy model with *Generalized IC* adequately represents the underlying physical processes once the REV-scale information is available only.

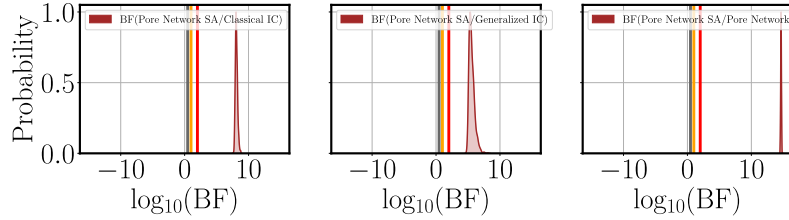


Figure 16. Distributions of \log_{10} (Bayes factor) of the *Pore-Network* model, with the surface averaging against competing models based on the validation scenario.

In addition to the setup presented in Section 4.1, we also analyzed two other cases. Firstly, we considered a setup with the same geometrical configuration, but the inlet boundary was located at the left domain edge in the free-flow region with an opening of 1.5 mm from the top. This setup induces a flow profile parallel to the interface. Comparing *Classical IC* with *Generalized IC*, we witnessed no substantial evidence in favor of any model. This observation is in line with the results from (Eggenweiler & Rybak, 2021), where the authors showed that the Stokes–Darcy problem with *Classical IC* and *Generalized IC* provides similar simulation results for parallel flows to the porous layer (Eggenweiler & Rybak, 2021). The second additional setup is based on the same flow models and boundary conditions as presented in Section 4.1, however, the solid inclusions are circular. We compared the Stokes–Darcy model with *Classical IC* and *Generalized IC* against the reference data. The model comparison with Bayes Factor suggests strong evidence in favor of the *Generalized IC*, as expected and similar to the rectangular inclusions.

6 Summary and Conclusions

Models for coupling free flow with porous-medium flow contain various parametric uncertainties, particularly in the vicinity of the interface. We have offered a benchmark study that addresses not only these parametric uncertainties, but also conceptual modeling uncertainties due to different formulations of physical models. To do so, we have considered the Stokes equations coupled to different models for the porous-medium compartment and corresponding coupling strategies: the standard REV-scale model in form of Darcy’s law with classical or generalized interface conditions as well as the pore-network model. To quantify the potential uncertainties of these three models, we have applied a Bayesian uncertainty-aware validation framework that assesses the performance of each model with respect to the reference data. The reference data for velocities and pressure has been obtained via a fully resolved pore-scale model. Since the task of calibration and validation in a probabilistic manner requires many model evaluations, we have employed a model reduction technique, namely Bayesian Sparse Polynomial Chaos Expansion, to accelerate the calculations.

The advantage of employing this technique is that one can perform a sensitivity analysis without additional costs. This analysis is achieved using so-called Sobol indices that are derived analytically from the expansion coefficients. The application of the presented surrogate-assisted Bayesian uncertainty-aware framework is not limited to the investigated models considered in this manuscript but can be applied to many other applications.

Applying the suggested Bayesian validation framework, we have observed that matches between the predictions related to the considered models and the reference data are observed for the points in the deeper part of the porous medium for all coupled models. However, we have found differences in the predictive capabilities of the models in the vicinity of the interface and in the free-flow region. Moreover, we have propagated the post-calibration parametric uncertainty through each analyzed model to validate the different models against reference data that have not been used during the calibration phase. This uncertainty-aware Bayesian validation procedure has confirmed that the averaged pore-network model has the most difficulties representing the underlying physical process correctly. This issue is most likely due to the averaging approach used for the pore-network model, where velocities have to be calculated and interpolated from fluxes that are only given within pore throats. Moreover, addressing the differences in the predictions of the considered modeling concepts, we have performed a Bayesian model comparison. This comparison reveals that the Stokes–Darcy model with the generalized interface conditions represents processes on the REV scale best compared to the classical interface conditions and the correspondingly upscaled pore-network model. The pore-network model outperforms both Stokes–Darcy models with classical and generalized interface conditions only if the detailed pore-scale information is considered. We have also investigated two other cases: one with the opening boundary condition from left side and the other with circular inclusions in the porous medium. The analysis of the former setting, which induces parallel flow to the interface, reveals that the Stokes–Darcy models with the classical and the generalized interface conditions provide similar results. This observation was expected for flow parallel to the fluid–porous interface. The findings of the analysis for the setup with circular inclusions confirms that there is decisive evidence in favor of the generalized interface condition to be superior to the classical interface. Concluding, we have observed that the suggested surrogate-assisted uncertainty-aware Bayesian validation framework helps to gain insight into underlying physical processes at considerably low computational costs.

Acknowledgments

The work is funded by the Deutsche Forschungsgemeinschaft (DFG, German Research Foundation) – Project Number 327154368 – SFB 1313. The Bayesian framework and the models’ source codes, as well as the reference data used in this study, are available at <https://git.iws.uni-stuttgart.de/dumux-pub/mohammadi2022a>.

References

- Angluin, D., & Smith, C. H. (1983). Inductive inference: theory and methods. *ACM Comput. Surv.*, 15(3), 237–269.
- Angot, P., Goyeau, B., & Ochoa-Tapia, J. A. (2017). Asymptotic modeling of transport phenomena at the interface between a fluid and a porous layer: jump conditions. *Phys. Rev. E*, 95, 063302.
- Angot, P., Goyeau, B., & Ochoa-Tapia, J. A. (2021). A nonlinear asymptotic model for the inertial flow at a fluid-porous interface. *Adv. Water Res.*, 149, 103798.
- Arjouni, Y., Kaabouch, N., El Ghazi, H., & Tamtaoui, A. (2017). Compressive sensing: performance comparison of sparse recovery algorithms. In *2017 IEEE 7th annual computing and communication workshop and conference (CCWC)*

- (pp. 1–7).
- Balhoff, M. T., Thomas, S. G., & Wheeler, M. F. (2007). Mortar coupling and up-scaling of pore-scale models. *Comput. Geosci.*, *12*(1), 15–27.
- Balhoff, M. T., Thompson, K. E., & Hjortsø, M. (2007). Coupling pore-scale networks to continuum-scale models of porous media. *Comput. Geosci.*, *33*(3), 393–410.
- Bayarri, M. J., Berger, J. O., Paulo, R., Sacks, J., Cafeo, J. A., Cavendish, J., ... Tu, J. (2007). A framework for validation of computer models. *Technometrics*, *49*(2), 138–154.
- Bazargan, H., & Christie, M. (2017). Bayesian model selection for complex geological structures using polynomial chaos proxy. *Comput. Geosci.*, *21*(3), 533–551.
- Bazargan, H., Christie, M., Elsheikh, A. H., & Ahmadi, M. (2015). Surrogate accelerated sampling of reservoir models with complex structures using sparse polynomial chaos expansion. *Adv. Water Resour.*, *86*, 385–399.
- Beavers, G. S., & Joseph, D. D. (1967). Boundary conditions at a naturally permeable wall. *J. Fluid Mech.*, *30*, 197–207.
- Beckers, F., Heredia, A., Noack, M., Nowak, W., Wieprecht, S., & Oladyskhin, S. (2020). Bayesian calibration and validation of a large-scale and time-demanding sediment transport model. *Water Resources Research*, *56*(7), e2019WR026966.
- Berger, J. O. (2013). *Statistical decision theory and Bayesian analysis*. Springer Science & Business Media.
- Beyhaghi, S., Xu, Z., & Pillai, K. M. (2016). Achieving the inside–outside coupling during network simulation of isothermal drying of a porous medium in a turbulent flow. *Transp. Porous Media*, *114*(3), 823–842.
- Blunt, M. J. (2017). *Multiphase flow in permeable media: a pore-scale perspective*. Cambridge University Press.
- Brynjarsdóttir, J., & O’Hagan, A. (2014). Learning about physical parameters: The importance of model discrepancy. *Inverse problems*, *30*(11), 114007.
- Carraro, T., Goll, C., Marciniak-Czochra, A., & Mikelić, A. (2015). Effective interface conditions for the forced infiltration of a viscous fluid into a porous medium using homogenization. *Comput. Methods Appl. Mech. Engrg.*, *292*, 195–220.
- Discacciati, M., & Gerardo-Giorda, L. (2018). Optimized Schwarz methods for the Stokes–Darcy coupling. *IMA J. Numer. Anal.*, *38*, 1959–1983.
- Discacciati, M., Miglio, E., & Quarteroni, A. (2002). Mathematical and numerical models for coupling surface and groundwater flows. *Appl. Num. Math.*, *43*, 57–74.
- Discacciati, M., & Quarteroni, A. (2009). Navier–Stokes/Darcy coupling: modeling, analysis, and numerical approximation. *Rev. Mat. Complut.*, *22*, 315–426.
- Draper, D. (1995). Assessment and propagation of model uncertainty. *J. R. Stat. Soc. Ser. B. Stat. Methodol.*, *57*(1), 45–70.
- Eggenweiler, E., & Rybak, I. (2020). Unsuitability of the Beavers–Joseph interface condition for filtration problems. *J. Fluid Mech.*, *892*, A10.
- Eggenweiler, E., & Rybak, I. (2021). Effective coupling conditions for arbitrary flows in Stokes–Darcy systems. *Multiscale Model. Simul.*, *19*(2), 731–757.
- Elsheikh, A. H., Hoteit, I., & Wheeler, M. F. (2014). Efficient bayesian inference of subsurface flow models using nested sampling and sparse polynomial chaos surrogates. *Computer Methods in Applied Mechanics and Engineering*, *269*, 515–537.
- Foreman-Mackey, D., Farr, W. M., Sinha, M., Archibald, A. M., Hogg, D. W., Sanders, J. S., ... Pla, O. A. (2019). emcee v3: a Python ensemble sampling toolkit for affine-invariant MCMC. *J. Open Res. Software*, *4*(43), 1864.
- Gardner, P., Rogers, T., Lord, C., & Barthorpe, R. (2021). Learning model discrepancy: A Gaussian process and sampling-based approach. *Mech. Syst. Sig. Pro-*

- cess., 152, 107381.
- Gelman, A., Carlin, J. B., Stern, H. S., Dunson, D. B., Vehtari, A., & Rubin, D. B. (2013). *Bayesian data analysis*. CRC press.
- Geman, S., Bienenstock, E., & Doursat, R. (1992). Neural networks and the bias/variance dilemma. *Neural Comput.*, 4(1), 1–58.
- Goodman, J., & Weare, J. (2010). Ensemble samplers with affine invariance. *Commun. Appl. Math. Comput. Sci.*, 5(1), 65–80.
- Goyeau, B., Lhuillier, D., Gobin, D., & Velarde, M. (2003). Momentum transport at a fluid-porous interface. *Int. J. Heat Mass Transfer*, 46, 4071–4081.
- Hackbusch, W. (1989). On first and second order box schemes. *Computing*, 41(4), 277–296.
- Hanspal, N., Waghode, A., Nassehi, V., & Wakeman, R. (2009). Development of a predictive mathematical model for coupled Stokes/Darcy flows in cross-flow membrane filtration. *Chem. Eng. J.*, 149, 132–142.
- Harlow, F. H., & Welch, J. E. (1965). Numerical calculation of time-dependent viscous incompressible flow of fluid with free surface. *Phys. Fluids*, 8(12), 2182–2189.
- Hills, R. G. (2006). Model validation: model parameter and measurement uncertainty. *J. Heat Transfer*, 128(4), 339–351.
- Hoeting, J. A., Madigan, D., Raftery, A. E., & Volinsky, C. T. (1999). Bayesian model averaging: a tutorial. *Statist. Sci.*, 14(4), 382–417.
- Hornung, U. (1997). *Homogenization and porous media*. Springer.
- Iooss, B., & Lemaître, P. (2015). A review on global sensitivity analysis methods. In G. Dellino & C. Meloni (Eds.), *Uncertainty management in simulation-optimization of complex systems: Algorithms and applications* (pp. 101–122). Springer.
- Jäger, W., & Mikelić, A. (2000). On the interface boundary conditions by Beavers, Joseph and Saffman. *SIAM J. Appl. Math.*, 60, 1111–1127.
- Jäger, W., & Mikelić, A. (2009). Modeling effective interface laws for transport phenomena between an unconfined fluid and a porous medium using homogenization. *Transp. Porous Media*, 78, 489–508.
- Jeffreys, H. (1961). *The theory of probability*. Oxford University Press.
- Kass, R. E., & Raftery, A. E. (1995). Bayes factors. *J. Amer. Statist. Assoc.*, 90(430), 773–795.
- Kennedy, M. C., & O’Hagan, A. (2001). Bayesian calibration of computer models. *J. R. Stat. Soc. Series B (Statistical Methodology)*, 63(3), 425–464.
- Koch, T., Gläser, D., Weishaupt, K., Ackermann, S., Beck, M., Becker, B., . . . Flemisch, B. (2021). Dumux 3—an open-source simulator for solving flow and transport problems in porous media with a focus on model coupling. *Comput. Math. Appl.*, 81, 423–443.
- Koch, T., Weishaupt, K., Müller, J., Weigand, B., & Helmig, R. (2021, Oct 01). A (dual) network model for heat transfer in porous media. *Transp. Porous Media*, 140(1), 107–141.
- Lācis, U., & Bagheri, S. (2017). A framework for computing effective boundary conditions at the interface between free fluid and a porous medium. *J. Fluid Mech.*, 812, 866–889.
- Lācis, U., Sudhakar, Y., Pasche, S., & Bagheri, S. (2020). Transfer of mass and momentum at rough and porous surfaces. *J. Fluid Mech.*, 884, A21.
- Le Bars, M., & Worster, M. (2006). Interfacial conditions between a pure fluid and a porous medium: implications for binary alloy solidification. *J. Fluid Mech.*, 550, 149–173.
- Ling, Y., Mullins, J., & Mahadevan, S. (2014). Selection of model discrepancy priors in Bayesian calibration. *J. Comput. Phys.*, 276, 665–680.
- Liu, J. S. (2008). *Monte Carlo strategies in scientific computing*. Springer Science & Business Media.

- Lüthen, N., Marelli, S., & Sudret, B. (2021). Sparse polynomial chaos expansions: literature survey and benchmark. *SIAM/ASA J. Uncertainty Quantif.*, 9(2), 593–649.
- Mahadevan, S., & Rebba, R. (2005). Validation of reliability computational models using bayes networks. *Reliab. Eng. Syst. Saf.*, 87(2), 223–232.
- Marelli, S., Lüthen, N., & Sudret, B. (2021). *UQLab user manual–Polynomial chaos expansions* (Tech. Rep. No. UQLab-V1.4-104). Chair of Risk, Safety and Uncertainty Quantification, ETH Zurich, Switzerland.
- Mehmani, Y., & Balhoff, M. T. (2014). Bridging from pore to continuum: a hybrid mortar domain decomposition framework for subsurface flow and transport. *Multiscale Model. Simul.*, 12(2), 667–693.
- Mehmani, Y., & Tchelepi, H. A. (2017). Minimum requirements for predictive pore-network modeling of solute transport in micromodels. *Adv. Water Resour.*, 108, 83–98.
- Mierzwiczak, M., Fraska, A., & Grabski, J. (2019). Determination of the slip constant in the Beavers–Joseph experiment for laminar fluid flow through porous media using a meshless method. *Math. Probl. Eng.*, 2019, 1494215.
- Mohammadi, F. (2020). *Development and realization of validation benchmarks*. (<https://arxiv.org/abs/2011.13216>)
- Mohammadi, F., Kopmann, R., Guthke, A., Oladyshkin, S., & Nowak, W. (2018). Bayesian selection of hydro-morphodynamic models under computational time constraints. *Adv. Water Resour.*, 117, 53–64.
- Oberkampf, W. L., & Barone, M. F. (2006). Measures of agreement between computation and experiment: validation metrics. *J. Comput. Phys.*, 217(1), 5–36.
- Oberkampf, W. L., & Roy, C. J. (2010). *Verification and validation in scientific computing*. Cambridge University Press.
- Oberkampf, W. L., & Trucano, T. G. (2008). Verification and validation benchmarks. *Nucl. Eng. Des.*, 238, 716–743.
- Ochoa-Tapia, A. J., & Whitaker, S. (1995). Momentum transfer at the boundary between a porous medium and a homogeneous fluid. I: theoretical development. *Int. J. Heat Mass Transfer*, 38, 2635–2646.
- Oladyshkin, S., De Barros, F., & Nowak, W. (2012). Global sensitivity analysis: a flexible and efficient framework with an example from stochastic hydrogeology. *Adv. Water Resour.*, 37, 10–22.
- Oladyshkin, S., Mohammadi, F., Kroeker, I., & Nowak, W. (2020). Bayesian3 active learning for the Gaussian process emulator using information theory. *Entropy*, 22(8), 890.
- Oladyshkin, S., & Nowak, W. (2012). Data-driven uncertainty quantification using the arbitrary polynomial chaos expansion. *Reliab. Eng. Syst. Saf.*, 106, 179–190.
- Oladyshkin, S., & Nowak, W. (2018). Incomplete statistical information limits the utility of high-order polynomial chaos expansions. *Reliab. Eng. Syst. Saf.*, 169, 137–148.
- Oladyshkin, S., & Nowak, W. (2019). The connection between Bayesian inference and information theory for model selection, information gain and experimental design. *Entropy*, 21(11), 1081.
- Oostrom, M., Mehmani, Y., Romero-Gomez, P., Tang, Y., Liu, H., Yoon, H., . . . Zhang, C. (2016). Pore-scale and continuum simulations of solute transport micromodel benchmark experiments. *Comput. Geosci.*, 20(4), 857–879.
- Patzek, T. W., & Silin, D. B. (2001). Shape factor and hydraulic conductance in noncircular capillaries: I. One-phase creeping flow. *J. Colloid Interface Sci.*, 236, 295–304.
- Robert, C., & Casella, G. (2013). *Monte Carlo statistical methods*. Springer Science & Business Media.

- Roy, C. J. (2019). Errors and uncertainties: their sources and treatment. In *Computer simulation validation* (pp. 119–141). Springer.
- Rybak, I., Schwarzmeier, C., Eggenweiler, E., & Rüde, U. (2021). Validation and calibration of coupled porous-medium and free-flow problems using pore-scale resolved models. *Comput. Geosci.*, *25*(2), 621–635.
- Saffman, P. G. (1971). On the boundary condition at the surface of a porous medium. *Stud. Appl. Math.*, *50*, 93–101.
- Scheibe, T. D., Murphy, E. M., Chen, X., Rice, A. K., Carroll, K. C., Palmer, B. J., ... Wood, B. D. (2015). An analysis platform for multiscale hydrogeologic modeling with emphasis on hybrid multiscale methods. *Groundwater*, *53*(1), 38–56.
- Scheurer, S., Schäfer Rodrigues Silva, A., Mohammadi, F., Hommel, J., Oladyshkin, S., Flemisch, B., & Nowak, W. (2021). Surrogate-based bayesian comparison of computationally expensive models: application to microbially induced calcite precipitation. *Comput. Geosci.*, *25*(6), 1899–1917.
- Schneider, M., Gläser, D., Weishaupt, K., Coltman, E., Flemisch, B., & Helmig, R. (2021). *Coupling staggered-grid and vertex-centered finite-volume methods for coupled porous-medium free-flow problems*. (<https://arxiv.org/abs/2112.11089>)
- Schöniger, A., Wöhling, T., & Nowak, W. (2015). A statistical concept to assess the uncertainty in Bayesian model weights and its impact on model ranking. *Water Resour. Res.*, *51*(9), 7524–7546.
- Schöniger, A., Wöhling, T., Samaniego, L., & Nowak, W. (2014). Model selection on solid ground: rigorous comparison of nine ways to evaluate Bayesian model evidence. *Water Resour. Res.*, *50*(12), 9484–9513.
- Smith, A. F., & Gelfand, A. E. (1992). Bayesian statistics without tears: a sampling-resampling perspective. *Am. Stat.*, *46*(2), 84–88.
- Sobol', I. (1993). Sensitivity estimates for nonlinear mathematical models. *Math. Model. Comput. Exp.*, *1*(4), 407–414.
- Sokal, A. D. (1996). Monte Carlo Methods in Statistical Mechanics: Foundations and New Algorithms Note to the Reader. In *Functional integration* (pp. 131–192).
- Sudret, B. (2008). Global sensitivity analysis using polynomial chaos expansions. *Reliab. Eng. Syst. Saf.*, *93*(7), 964–979.
- Terzis, A., Zarikos, I., Weishaupt, K., Yang, G., Chu, X., Helmig, R., & Weigand, B. (2019). Microscopic velocity field measurements inside a regular porous medium adjacent to a low Reynolds number channel flow. *Phys. Fluids*, *31*, 042001.
- Tipping, M. E. (2001). Sparse Bayesian learning and the relevance vector machine. *J. Mach. Learn. Res.*, *1*(3), 211–244.
- Tipping, M. E., & Faul, A. (2003). Fast marginal likelihood maximisation for sparse Bayesian models. In *Proceedings of the 9th international workshop on artificial intelligence and statistics* (pp. 3–6).
- Wagner, P.-R., Nagel, J., Marelli, S., & Sudret, B. (2021). *UQLab user manual – Bayesian inversion for model calibration and validation* (Tech. Rep. No. UQLab-V1.4-113). Chair of Risk, Safety and Uncertainty Quantification, ETH Zurich, Switzerland.
- Weishaupt, K., Joekar-Niasar, V., & Helmig, R. (2019). An efficient coupling of free flow and porous media flow using the pore-network modeling approach. *J. Comput. Phys.*, *1*, 100011.
- Weishaupt, K., Terzis, A., Zarikos, I., Yang, G., Flemisch, B., de Winter, D. A. M., & Helmig, R. (2020). A hybrid-dimensional coupled pore-network/free-flow model including pore-scale slip and its application to a micromodel experiment. *Transp. Porous Media*, *135*(1), 243–270.
- Wiener, N. (1938). The homogeneous chaos. *Am. J. Math.*, *60*(4), 897–936.

- Xu, T., & Valocchi, A. J. (2015). A Bayesian approach to improved calibration and prediction of groundwater models with structural error. *Water Resour. Res.*, *51*(11), 9290–9311.
- Yang, G., Coltman, E., Weishaupt, K., Terzis, A., Helmig, R., & Weigand, B. (2019). On the Beavers–Joseph interface condition for non-parallel coupled channel flow over a porous structure at high Reynolds numbers. *Transp. Porous Media*, *128*, 431–457.
- Yoon, H. N., Marshall, L., Sharma, A., & Kim, S. (2022). Bayesian model calibration using surrogate streamflow in ungauged catchments. *Water Resour. Res.*, *58*(1), e2021WR031287.
- Zampogna, G. A., & Bottaro, A. (2016). Fluid flow over and through a regular bundle of rigid fibres. *J. Fluid Mech.*, *792*, 5–35.